AD-A170 506   ACCELERATION PROCESSES IN THE EARTH'S MAGNETOSPHERE(U)   1/1
CALIFORNIA UNIV LOS ANGELES INST OF GEOPHYSICS AND
PLANETARY PHYSICS   M ASHOUR-ABDALLA ET AL. 17 MAY 85
UNCLASSIFIED   AFGL-TR-85-0143 F19628-82-K-0019   F/G 4/1   NL

AFGL-TR-85-0143

Acceleration Processes in the Earth's Magnetosphere

M. Ashour-Abdalla   C. F. Kennel
P. J. Coleman, Jr   J. N. Leboeuf
J. M. Dawson   H. Okuda
W. Gekelman   R. Stenzel
                           R. J. Walker

University of California, Los Angeles
Institute of Geophysics & Planetary Physics
Los Angeles, CA 90024

Final Report
December 1981 - December 1984

17 May 1985

AIR FORCE GEOPHYSICS LABORATORY
AIR FORCE SYSTEMS COMMAND
UNITED STATES AIR FORCE
HANSCOM AIR FORCE BASE, MASSACHUSETTS 01731

AD-A170 506

DTIC FILE COPY

DTIC
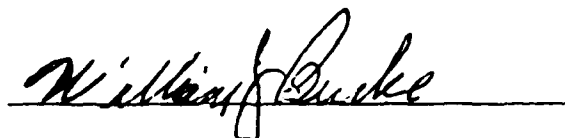ELECTE
AUG 0 4 1986
D

86   8   4   003

SAMPLE FOR CONTRACTOR REPORTS

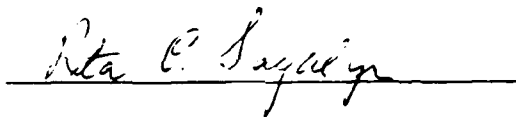"This technical report has been reviewed and is approved for publication"

DELIA E. DONATELLI
Contract Manager

WILLIAM J. BURKE
Branch Chief

FOR THE COMMANDER

RITA C. SAGALYN
Division Director

This report has been reviewed by the ESD Public Affairs Office (PA) and is releasable to the National Technical Information Service (NTIS).

Qualified requestors may obtain additional copies from the Defense Technical Information Center. All others should apply to the National Technical Information Service.

ADA159456

REPORT DOCUMENTATION PAGE

1a. REPORT SECURITY CLASSIFICATION		1b. RESTRICTIVE MARKINGS		
Unclassified				
2a. SECURITY CLASSIFICATION AUTHORITY		3. DISTRIBUTION/AVAILABILITY OF REPORT		
		APPROVED FOR PUBLIC RELEASE; DISTRIBUTION UNLIMITED.		
2b. DECLASSIFICATION/DOWNGRADING SCHEDULE				
4. PERFORMING ORGANIZATION REPORT NUMBER(S)		5. MONITORING ORGANIZATION REPORT NUMBER(S)		
		AFGL-TR-85-0143		
6a. NAME OF PERFORMING ORGANIZATION	6b. OFFICE SYMBOL (If applicable)	7a. NAME OF MONITORING ORGANIZATION		
University of California, Los Angeles		Air Force Geophysics Laboratory		
6c. ADDRESS (City, State and ZIP Code)		7b. ADDRESS (City, State and ZIP Code)		
Institute of Geophysics & Planetary Physics Los Angeles, CA 90024		Hanscom AFB Massachusetts 01731		
8a. NAME OF FUNDING/SPONSORING ORGANIZATION	8b. OFFICE SYMBOL (If applicable)	9. PROCUREMENT INSTRUMENT IDENTIFICATION NUMBER		
		F19628-82-K-0019		
8c. ADDRESS (City, State and ZIP Code)		10. SOURCE OF FUNDING NOS		

		PROGRAM ELEMENT NO	PROJECT NO	TASK NO	WORK UNIT NO
11. TITLE (Include Security Classification) Acceleration Processes in the Earth's Magnetosphere		62101F	7601	17	AA

12. PERSONAL AUTHOR(S) H. Okuda, R. Stenzel, R.J. Walker
M. Ashour-Abdalla, P.J. Coleman, J.M. Dawson, W. Gekelman, C.F. Kennel, J.N. Leboeut,

13a. TYPE OF REPORT	13b. TIME COVERED	14. DATE OF REPORT Yr., Mo., Day	15. PAGE COUNT
FINAL	FROM Dec 1981 TO Dec 1984	17 May 1985	102

16. SUPPLEMENTARY NOTATION

17. COSATI CODES			18. SUBJECT TERMS (Continue on reverse if necessary and identify by block number)
FIELD	GROUP	SUB GR	Acceleration of Heavy Ions
			Magnetic Reconnection
			Magnetosphere-Ionosphere Coupling

19. ABSTRACT (Continue on reverse if necessary and identify by block number)

Three main topics have been concentrated on in this study:

1) Acceleration of heavy ions on auroral field lines and in the ring current;

2) Kinetic and magnetohydrodynamic studies of reconnection processes in the earth's magnetosphere; and

3) The coupling of the magnetosphere and ionosphere via field aligned currents.

Included here is a list of publications that have resulted from the above research. Two additional reports are presented here: "Driven Magnetic Reconnection in Three Dimensions: Energy Conversion and Field Aligned Current Generation" by Tetsuya Sato, Raymond J. Walker

20. DISTRIBUTION/AVAILABILITY OF ABSTRACT	21. ABSTRACT SECURITY CLASSIFICATION	
UNCLASSIFIED/UNLIMITED ☐ SAME AS RPT ☐ DTIC USERS ☐	Unclassified	
22a. NAME OF RESPONSIBLE INDIVIDUAL	22b. TELEPHONE NUMBER (Include Area Code)	22c. OFFICE SYMBOL
Delia E. Donatelli	(617) 377-3103	AFGL/PHA

DD FORM 1473, 83 APR EDITION OF 1 JAN 73 IS OBSOLETE

Block 19 (Cont)

and Maha Ashour-Abdalla; and "Heating of Thermal Helium in the Equatorial Magnetosphere:

A Simulation Study" by Y. Omura, M. Ashour Abdalla, K. Quest, and R. Gendrin.

Table of Contents

Accesion For

Accesion For		
NTIS CRA&I	☑	
DTIC TAB	☐	
U:iannounced	☐	
Justification		
By		
Di:t ibution /		
Availability Codes		
Dist	Avail and/or Special	
A-1		

DRIVEN MAGNETIC RECONNECTION IN THREE DIMENSIONS:

ENERGY CONVERSION AND

FIELD ALIGNED CURRENT GENERATION

Tetsuya Sato,[1,2]

Raymond J. Walker[1] and Maha Ashour-Abdalla[1]

[1]Institute of Geophysics and Planetary Physics
University of California
Los Angeles, California 90024

[2]Institute for Fusion Theory
Hiroshima University
Hiroshima 730, Japan

Acknowledgements

ABSTRACT

We have analyzed the energy conversion processes occurring in three dimensional driven reconnection. In particular, we studied the energy conversion processes during localized reconnection in a tail like magnetic configuration. We find that 3D driven reconnection is a powerful energy converter which transforms magnetic energy into plasma bulk flow and thermal energy. Three dimensional driven reconnection is an even more powerful energy converter than 2D reconnection because in the 3D case plasmas were drawn into the reconnection region from the sides as well as from the top and bottom. Field aligned currents are generated by 3D driven reconnection. We have identified the physical mechanism responsible for these currents which flow from the tail toward the ionosphere on the dawn side of the reconnection region and from the ionosphere towards the tail on the dusk side. The field aligned currents form as the neutral sheet current is diverted through the slow shocks which form on the outer edge of the reconnected field lines (outer edge of the plasma sheet).

5

1. INTRODUCTION

A magnetospheric substorm is a good example of an explosive energy conversion process in cosmical plasmas. Over the past two decades, two models of the substorm have evolved, the unloading model or energy storage and release model and the driven model. In the unloading model, reconnection on the dayside magnetopause leads to enhanced convection and the storage of magnetic energy in the magnetotail magnetic field (McPherron et al., 1973; Russell and McPherron, 1973). This leads to thinning of the near earth plasma sheet and to the formation of a new neutral line in a localized region in the near-earth ($10 \sim 15$ R_E) plasma sheet (McPherron et al., 1973; Russell and McPherron, 1973; Hones, 1973). This reconnection impulsively releases the stored energy at substorm onset to power geomagnetic activity. The driven model, too, starts with magnetic merging on the dayside magnetopause. However, in this model the magnetosphere responds directly to variations in the external solar wind conditions (Perreault and Akasofu, 1978; Akasofu, 1979, 1980). In particular, the energy input rate from the solar wind equals the energy output rate during the substorm in the driven model.

In this paper, we present a three-dimensional model of tail reconnection during substorms. Our primary purpose is to study the energy conversion processes occurring in the tail. When we wish to contruct a sound physical model to explain any naturally occurring phenomenon, it is essential to understand the fact that the system is energetically "open". To reveal an energy conversion process, the first step we take is to extract a portion (black box) out of the causal chain in which the process we are concerned with is taking place. The black box must be extracted so that there is little feedback of energy from the output to input during the course of the energy conversion. Otherwise, the model, no matter how mathematically sound, is physically

unacceptable. If the black box is so small that a substantial part of the output energy returns to the input on the time scale of interest, then the model obviously includes an internal inconsistency. The model must be expanded so that the output energy returning to the input can be included. On the other hand, if the black box is so large that several separable energy conversion processes are included, then the model is acceptable. The global simulation of the magnetosphere is an example of such a system and in principle is the preferred way to study the substorm process. However, because of the limitations of the available computers, the model is often so coarse-grained that the physical process underlying the energy conversion can be overlooked. In order to comprehend the physical process, therefore, it is desirable to divide this black box into self-consistent, smaller boxes.

In a substorm, a substantial part of the energy output is lost in the ionosphere. The lost energy goes into the heating of neutral atoms and molecules, so that it is unlikely that the lost energy goes back to the magnetosphere during the course of a substorm. On the other hand, similar substorms are observed repeatedly. From the repeatability of substorms and the existence of definite energy loss in the ionosphere, we can conclude that there must exist a finite energy input to the system. Accordingly, a model substorm must be constructed to include a proper input and output. From causality, the input must change the conditions within the black box in such a way that a substorm is triggered.

We have designed our model to investigate the effects of convection on the initiation of tail reconnection. In this driven reconnection model, reconnection results from flow from the lobes normal to the neutral sheet (Sato, 1979). In order to have sufficient resolution in the model, we consider only a small volume around the reconnection region. The input from the solar wind is

determined by the boundary conditions at the top and bottom of the simulation box. The term driven when applied to reconnection does not have the same meaning as when it is used to describe phenomenological models of substorms. As we will see in this study, driven reconnection is an active energy converter in which magnetic energy stored in the tail lobes is converted into plasma energy. Thus the driven reconnection model is similar to the unloading model of substorms.

II. GENERAL REMARKS ON ENERGY CONVERSION

Deriving the energy equations from the ordinary set of resistive magneto-hydrodynamic (MHD) equations, we obtain

$$\frac{\partial K}{\partial t} = - \int \frac{1}{2} \rho v^2 \underline{v} \cdot d\underline{S} + \int \underline{J} \times \underline{B} \cdot \underline{v}dV - \int \nabla p \cdot \underline{v}dV \tag{1}$$

$$\frac{\partial T}{\partial t} = - \int \frac{\gamma}{\gamma-1} p\underline{v} \cdot d\underline{S} + \int \nabla p \cdot \underline{v}dV + \int \eta J^2 dV \tag{2}$$

$$\frac{\partial W}{\partial t} = - \int \frac{\underline{E} \times \underline{B}}{\mu_0} \cdot d\underline{S} - \int \underline{J} \times \underline{B} \cdot \underline{v}dV - \int \eta J^2 dV \tag{3}$$

where

$$K = \int \frac{1}{2} \rho v^2 dV \quad \text{(kinetic energy)} \tag{4}$$

$$T = \int \frac{p}{\gamma-1} dV \quad \text{(thermal energy)} \tag{5}$$

$$W = \int \frac{B^2}{2\mu_0} dV \quad \text{(magnetic energy)} \tag{6}$$

and $d\underline{S}$ is the surface element vector and dV is the volume element. In (1)-(6), ρ is the mass density, v is the velocity, J is the current density, B is the magnetic field, p is the pressure, γ is the polytropic index, η is the resistivity, and E is the electric field.

These equations give us all the necessary information about the macroscopic energy conversion in a black box. The left-hand sides of (1)-(3) represent the changes in the total kinetic, thermal and magnetic energies in the black box. The first terms on the right represent the output and input powers of the black box. As described in the introduction, the input power is essential in the present model since it is responsible for the change in the initial equilibrium configuration which triggers an energy conversion process in the black box. The output power provides a key to the energy conversion process because we are interested in how much energy is ejected from the black box as a consequence of the conversion.

10

The last two terms on the right-hand sides of (1)-(3) represent the mutual energy exchanges among the kinetic, thermal and magnetic energies inside the black box. They can give us information about the efficiency of the energy conversion process. They can be used to answer questions such as how quickly the magnetic energy is converted into kinetic energy. As a consequence of this internal conversion, the internal energy is ejected out of the black box. The ejected (output) energy can in turn be an input energy for the succeeding event in the external causal chain. For instance in the magnetospheric substorm, this succeeding event can be the excitation of auroras.

A diagram of energy conversion processes is shown in Figure 1.

III. EXTERNALLY DRIVEN RECONNECTION

In the reconnection process the energy source to be released is the magnetic energy. In the magnetotail, the magnetic energy consists of two components. One is the dipole field and the other is the field produced by the diamagnetic current flowing in the plasma sheet. The dipole field is a potential field and cannot be released at all. The only free energy is the magnetic energy stored in the diamagnetic currents which deform the dipole to form the tail. Thus an external energy agent such as the solar wind which deforms the magnetosphere must play a leading role in triggering reconnection in the plasma sheet.

It would be natural, therefore, to presume that the solar wind intruding into the magnetosphere through dayside reconnection could drive reconnection in the magnetotail. The intruding solar wind effects the tail in two ways. First, the magnetic free energy is stored in the plasma sheet. This is manifested as a plasma sheet thinning. Second, the invading plasma triggers reconnection by compressing the plasma sheet. To approximate this process, we developed the driven reconnection model [Hayashi and Sato, 1978; Sato et al., 1978; Sato and Hayashi, 1979; Sato, 1979; Sato et al., 1983].

Indeed, this idea that reconnection would occur somewhere in the magnetotail has been demonstrated by global simulations of the solar wind-magnetosphere interaction [Leboeuf et al., 1981; Brecht et al., 1953; Wu, 1983].

12

IV. NUMERICAL MODEL

The numerical model has been described previously [Sato et al., 1953; Sato and Hayashi, 1982]. Here we will summarize it briefly for convenience. We started with a very simple equilibrium configuration. The magnetic field and plasma configurations we used are

$$\underline{B}(x,y,z) = (B_0 \tanh(z/L), 0, 0)$$

$$\rho(x,y,z) = \rho_0$$

$$T(x,y,z) = T_0 \operatorname{sech}^2(z/L)$$

where $\underline{B}$ is the magnetic field, ρ is the mass density, T is the temperature, B_0, ρ_0, T_0 are constants and L is the half-width of the neutral sheet in the z (north-south) direction.

We assumed that reconnection is triggered by a non-uniform compression of the plasma sheet. In order to compress the plasma sheet, we injected a magnetized plasma through the north and south boundary planes ($z = \pm L_z$) of the simulation box. Initially, the incoming mass flow pattern was such that

$$\rho v_z(z = \pm L_z) = \mp \frac{A_0}{4} (1 + \cos \frac{\pi x}{L_x})(1 + \cos \frac{\pi y}{L_y})$$

where v_z is the z-component of the velocity, L_x, L_y, L_z are the dimensions of the simulation box and A_0 is a constant. ρv_x and ρv_y were initially set to zero. Later they were adjusted so that the mass flow vector was always perpendicular to $\underline{B}$ at the boundary. The other boundaries ($x = \pm L_x$ and $y = L_y$) were open boundaries through which plasmas can freely enter or exit. We reduced the physical domain of the simulation box by assuming symmetry (or anti-symmetry when appropriate) about the equator ($z=0$), the noon-midnight meridian ($y=0$) and the neutral line ($x=0$). We have adopted the resistivity (η) model [Sato, 1979]

$$\eta = \alpha(V_D - V_c)^2 \text{ for } V_D > V_c$$

13

where V_D is the diamagnetic drift velocity and α and V_c are constants. $V_D = J/ne$ where J is the neutral sheet current, n is the plasma density and e is the electron charge.

The simulation system was a rectangular box with dimension $L_x = 3L$, $L_y = 5L$ and $L_z = 2L$. This was implemented on a $41 \times 40 \times 51$ point grid.

In the actual calculations, all variables were normalized to the following parameters: L, Length; $V_A = \frac{B_0}{(\mu_0 \rho_0)}1/2$, velocity; B_0, magnetic field; ρ_0, mass density; $B_0/\mu_0 L$, current; $B_0^2/2\mu_0$, pressure; B_0^2/μ_0, energy; $\gamma_0 L V_A$, resistivity; and $B_0 V_A$, electric field. In the computer run presented here we set $A_0 = .2$, $\alpha = 0.02$ and $V_c = 3$ while B_0, T_0, ρ_0 and V_D were all normalized to 1.

V. NUMERICAL RESULTS

In the 2D model, only the compressional magnetohydrodynamic modes, the fast and slow modes, can be taken into account, but the shear Alfvén mode cannot. Consequently, no field aligned currents can be modeled because it is the Alfvén wave that can carry the field aligned current. In order to model field aligned currents, a 3D model is necessary.

That field aligned currents can be generated by 3D externally driven reconnection has been demonstrated by Sato et al. (1983). Starting with the MHD momentum equation, the continuity of current, mass continuity and the MHD approximation, the field aligned currents in the magnetosphere can be calculated by solving

$$B \frac{\partial}{\partial s}(\frac{v_{\parallel}}{B}) = \frac{2}{B} \underline{J}_{\perp} \cdot \nabla B - J_{in} \cdot \frac{\nabla N}{N} + c\rho \frac{d}{dt}(\frac{\Omega_{\parallel}}{B}) - \rho c[\Omega_{\perp} \cdot (b \cdot \nabla)\underline{v} + (\Omega_{\perp} \cdot \nabla_{\perp})\underline{v}] \quad (7)$$

with

$$\Omega = \nabla \times \underline{v}$$

$$\underline{J}_{\perp} = \underline{J}_D + \underline{J}_{in}$$

and

$$\underline{J}_D = c\underline{B} \times \nabla P/B^2$$

$$\underline{J}_{in} = c\underline{B} \times (\frac{\rho}{B^2} \frac{dv}{dt})$$

where $J_{\parallel}$ and $J_{\perp}$ are the parallel and perpendicular current densities, B is the magnetic field, ρ is the mass density, $\Omega_{\parallel}$ is the parallel component of Ω the vorticity, $\Omega_{\perp}$ is the perpendicular component of Ω, $\underline{J}_{in}$ is the inertia current, N is the density, P is the pressure and v is the velocity (Hasegawa and Sato, 1979; Sato and Iijima, 1979; Vasyliunas, 1984). The partial derivative on the left hand side of equation (7) is along $\underline{B}$. Sato (1982) has argued that the inertia current term is negligible and that the agent of the field aligned current must be the $J_{\perp} \cdot \nabla B$ term in equation (7). The diagram showing his pre-diction is reproduced in Figure 2.

15

He argued that as reconnection occurs in a localized region of the tail, two slow shocks will form into which the cross tail current will be diverted. In addition, B will increase at the slow shocks due to the pile up of field lines which are driven towards the neutral sheet. Thus, $J_\perp \cdot \nabla B > 0$ in the dawn sector and $J_\perp \cdot \nabla B < 0$ in the dusk sector. The resulting field aligned currents are directed from the tail towards the ionosphere on the dawn side and outward from the ionosphere towards the tail at dusk.

In this paper, we will use the simulation results to verify this prediction. Contours of the generated field aligned current intensity in two y-z cross sections ($x=2.25L$ and $x=3.0L$) are shown in Figures 3 and 4. For reference reconnection occurs at $x=0$. Two pairs of field aligned currents are generated: one is in the northern hemisphere ($z>0$) and the other is in the southern hemisphere ($z<0$). On the dawn side ($y<0$), the field aligned current flows from the magnetosphere towards the ionosphere, while on the dusk side it flows from the ionosphere towards the magnetosphere as predicted by the model. Two additional features should be noted in these figures. First, the field aligned current density is as large as the initial neutral sheet current density in a small region. This indicates that locally the neutral sheet current is almost completely interrupted. Secondly, the peak positions of the field aligned currents expand in the z-direction as the observation point moves along the x-axis away from the x line. This suggests that the field aligned current is generated at the slow shock layer [Sato et al., 1983].

In order to prove that the field aligned current originates from the $J_\perp \cdot \nabla B$ term, we have plotted the neutral sheet current $\underline{J}_\perp$ superimposed on the contours of the magnitude of the magnetic field B in Figure 5. If we examine the current distribution with care we find that the current density arrows in the equatorial plane ($z=0$) vanish at the edges of the reconnection region.

Furthermore, the divergence of the currents occurs across the B contours. In Figure 6 where we have overlapped Figures 4 and 5, we can clearly see that the contours of the field aligned current density coincide with the divergence of the neutral sheet current. The field aligned currents occur where $J_\perp \cdot \nabla B \neq 0$ as predicted by Sato's model. Note that the field aligned current density is very small ($J_\parallel < .02$) in the equatorial plane in the region where the cross tail current reverses direction. The field aligned currents are limited to the region of the slow shocks.

We also have investigated the contributions to $J_\parallel$ from the terms in (7) which are proportional to the vorticity, Ω. The parallel vorticity term gives a field aligned current which is opposite to that observed. Therefore, term (3) is not important for generating these currents. Both terms involving the perpendicular vorticity are appoximately zero and are much smaller than the first term. Thus we can conclude that the field aligned currents are generated by the $J_\perp \cdot \nabla B$ term.

In equilibrium the pressure contours are parallel to the magnetic field intensity contours. This means that the diamagnetic current, which is perpendicular to ∇p, must flow along an equi- B contour in an equilibrium. Thus, the field aligned current generation is due to the non-equilibrium magnetic field configuration caused by externally driven reconnection.

Generation of Super-Magnetosonic Flow

As noted above, externally driven reconnection produces slow shocks in which high-speed plasma flows are found [Sato, 1979]. In the 2D simulation, the flows reached the Alfvén velocity. The 3D simulation confirms a very similar behavior of plasma flow at least in the noon-midnight meridian plane [see Figure 2 of Sato et al., 1983]. In 3D, the plasma flow can become super-magnetosonic. In Figure 7, we have plotted the flow speed distribution (V_x) along the x-axis.

17

The curve V_F represents the distribution of the fast magnetosonic speed. The plasma flow is almost linearly accelerated along the x-axis from the reconnection region (x=0) up to about x=1. Since the velocity is normalized by the initial Alfven speed in the upstream region, we see that the speed well exceeds the Alfvén speed beyond x $\geq$ 1. The flow speed exceeds the local fast magnetosonic speed (V_F) beyond a certain point ($x > x_s$) and the local magnetosonic Mach number (V_x/V_F) reaches approximately 2. The local Mach number of the flow increases monotonically with distance beyond x_s. However, the absolute flow speed reaches a maximum at the super-magnetosonic point ($x=x_s$) and then decreases. This implies that some deceleration mechanism is operating beyond that point. The neutral sheet current density (J_y) distribution is plotted along the x-axis in Figure 8. For x $\geq$ 2, the current reverses direction (see also Figure 5 of Sato et al., (1983)). Since the reconnected field has a positive (northward) z-component in the positive x region, the $\underline{J} \times \underline{B}$ force points towards the x-point in the reversed current region and the plasma is decelerated in this region. This caused the velocity decrease in Figure 7. Sato et al. (1983), examined the currents in the equatorial plane and found a large current vortex between the reconnection region and the region of reconnected field lines. The current pattern in Figure 7 is along the symmetry axis of this vortex.

Let us now examine the corresponding distributions for the pressure (P) and the reconnected field B_z. There are two very important features in Figure 9. First, the reconnected field increases linearly with distance for x $\leq$ x_D. This is a clear indication of the diffusion region predicted by the steady reconnection theory [Petschek, 1964; Vasyliunas, 1975]. Note that the plasma is almost linearly accelerated as a function of x in this region (see Figure 7). The theory further predicts that beyond the diffusion region both the reconnected

field and the pressure should be constant in a region called the "wave" region. Such a plateau region is observed in the simulation for $x_D \lesssim x \lesssim x_s$. Most surprisingly, however, is a large, sharp decrease in the pressure profile at $x = x_s$. This is the point where the local magnetosonic Mach number exceeds one (see, Figure 7). A close examination of the B_z profile reveals that when the sharp drop in the pressure occurs, B_z also starts decreasing. Recall that the flow velocity decreases for $x > x_s$ (Figure 7). The steep decrease in pressure suggests that this may be a fast shock propagating in the positive x direction. However, there are difficulties with this interpretation. The density, which we would expect to decrease if this is a shock, increases ($\rho_{x=xs}/\rho_{x=2} = .99$). In addition, although the magnetic field decreases as we would expect, the decrease is very small ($B_{x=xs}/B_{x=2} = 1.03$).

Energy Conversion

In this section, we examine the energetics of 3D driven reconnection. Let us first examine the relationships between the input and output powers which are given by the first terms on the right-hand side of (1)-(3). Since there are three independent boundary planes, the output boundary (y-z), the side boundary (x-z) and the input boundary (x-y), we have 9 input and output power values to consider. These 9 values are plotted as a function of time in Figure 10. The three curves with the first three numbers, 1, 2 and 3, correspond to the kinetic energy. The three curves with the second three numbers, 4, 5 and 6, correspond to the thermal energy. The remaining three curves, 7, 8 and 9, correspond to the magnetic energy. The smallest number in each group, 1, 4 or 7, represents the output power through the output boundary. The middle number in each group, 2, 5 or 8, represents the output power through the side boundary. The last number, 3, 6 or 9, represents the input power through the input boundary.

19

A positive value for output power indicates that energy flows out through the boundary, while a negative value indicates that energy flows in. A positive value for the input power represents energy flow into the simulation region and a negative value represents outflow. From the input curves, 3, 6 and 9, we notice that most of the input power is carried by the magnetic field. This may well represent the actual magnetotail where the energy is accumulated predominantly in terms of the magnetic energy.

The input powers in 3, 6 and 9, stimulate reconnection and energy conversion in the black box. The resulting output kinetic, thermal and magnetic powers are shown by 1, 4 and 7. Since the induced super-magnetosonic flow is limited to the region within the two slow shock layers (i.e. the model plasma sheet), where the thermal energy is predominant, the dominant output power is the thermal power. The first rise in the thermal power (4) $(0 \lesssim t \lesssim 8\tau_A)$ is caused by the convection system set up in the black box from the input boundary. The second enhancement in the output power starting at $T \sim 8\tau_A$ is induced by reconnection. Coincident with this second rise in the thermal power, the kinetic power is greatly increased. In contrast, the change in the output magnetic power is not so remarkable. Since the output power caused by reconnection is limited to the slow shock regions, the calculation of the output power for this discussion also should be limited to the slow shock region. However, this does not change our conclusions since over 80% of the output power is within the slow shocks. Clearly, the total output power caused by reconnection exceeds the total input power. Thus, the energy conversion process occurring in the black box is an active process, not a simple pumping process induced by the input flow. Now let's look at the energy outputs through the side boundary, 2, 5 and 5. There is very little kinetic energy input or output (2). However, some power is pumped out of the black box through the side boundary early in the

simulation before reconnection has begun. During the reconnection stage, the power through the side boundary becomes negative. This means that the side boundary has become an energy source during reconnection. To clarify this we present the flow pattern in the y-z plane at x=0 (T=14.6) in Figure 1. Reconnection is occurring in the center of the figure. It is evident that plasma is being sucked into the reconnection region. This gives additional strong evidence that externally driven reconnection is a powerful energy converter. In the previous 2D simulations, no such phenomenon was allowed. This is a three-dimensional effect. It is this inflow through the side boundary which makes driven reconnection in three-dimensions a more powerful energy converter than that in two-dimensions. The fast shock-like structure observed in Figure 9 may be attributed to this effect of three-dimensionality.

In order to study the energy conversion, we need to examine the work done within the simulation box. There are three sources of work; the work done by the $\underline{J} \times \underline{B}$ force, the work done by the pressure force and the ohmic heating. These works are plotted in Figure 12. In the early pumping or convection stage $(0 \leq t \leq 8\tau_A)$, both the $\underline{J} \times \underline{B}$ force and the pressure force behave almost identically, which means that no net acceleration of plasma occurs. The oscillations are caused by the bouncing of the magnetosonic wave between the input boundaries. There is a marked difference in the curves during the reconnection stage $(t \geq 10\tau_A)$. The net difference goes into the acceleration of plasma at the expense of the magnetic energy. The small positive contribution of the pressure work implies that some adiabatic compression is occurring. In addition, ohmic heating contributes to the heating of the plasma during the reconnection period.

The temporal behavior of the total kinetic, thermal and magnetic energies are shown in Figure 13. Early in the simulation as the plasma flows from the input boundary toward the neutral sheet, the magnetic energy and the thermal

21

At the same time, the magnetic energy deviates from the linear growth. The differences of the magnetic and thermal energies from the initial linear growth line give the total amounts of energy ejected from the black box. Note that the kinetic energy starts to increase drastically in the reconnection stage.

VI. DISCUSSION AND CONCLUSIONS

Based on his 2D simulations, Sato (1979) argued that driven magnetic reconnection could be a powerful energy converter which transformed magnetic energy into plasma bulk flow and thermal energy. Such an explosive energy release mechanism is necessary to understand magnetospheric substorms or solar flares.

In this study, we have analyzed the energy conversion processes occurring in three-dimensional driven reconnection. In particular, we investigated the case in which reconnection occurred in a localized region in a tail-like magnetic configuration. Such localized reconnection is thought to occur in the magnetotail during substorms. We found that 3D driven reconnection is an even more powerful energy converter than the 2D case. This occurred because in the 3D case plasmas were drawn into the reconnection region from the sides as well as the top and bottom. In the 3D case, the flow velocity reached the magnetosonic velocity. It is interesting to note that the largest velocities occurred at the magnetosonic point with lower velocities farther from the reconnection region. We found that the neutral sheet current reversed signs in the region of reduced velocity so that the $\underline{J} \times \underline{B}$ force opposed the flow and decelerated the plasma.

As noted in the introduction, the term driven when applied to reconnection does not have the same meaning as when it is used to describe phenomenological models of substorms. Driven reconnection is an active energy converter in which magnetic energy is converted into plasma thermal energy and flow. In figure 10, the rate of at which energy is released is much faster than the rate at which energy is input into the model. Thus driven reconnection is similar to the unloading model of substorms in which magnetic energy stored in the tail lobes is converted into plasma energy.

Another important feature of the driven reconnection model is the formation of slow shocks near the outer edge of the reconnected field lines. The neutral

23

sheet current is diverted through the slow shocks. This leads to the generation of field aligned currents by the $J_\perp \cdot \nabla B$ term in equation (7). Sato et al. (1983) and Walker and Sato (1983) have compared the resulting current system with that inferred from observations of substorms in the tail. They found that the current system in Figures 3 and 4 with field aligned currents directed from the tail toward the earth on the dawn side and from the earth toward the tail at dusk is consistent with the current wedge model most frequently used to interpret substorm observations obtained near midnight.

We should note that Birn and Hones (1981) have done a similar calculation and find field aligned currents flowing in the opposite direction to those in Figures 3 and 4. In this model reconnection occurs following the initiation of anomalous resistivity in in the tail. Their model does not include the initial convection system characteristic of driven reconnection. These two models are not necessarily contradictory and it is possible that processes analogous to both operate in the tail during substorms. For instance, driven reconnection may initiate the substorm and then evolve into a process analogous to the Birn and Hones model. The two models are compared in greater detail in Walker and Sato (1984).

24

Figure Captions

Figure 1.   Schematic drawing of the energy conversion processes which can occur in driven reconnection.

Figure 2.   Schematic drawing of the plasma sheet during reconnection showing the generation of field aligned currents.

Figure 3.   Field aligned current density contours in the y-z (dawn-dusk) plane at x=2.25L at $T=14.6\tau_A$. The values on the contours are normalized to the initial neutral sheet current.

Figure 4.   Same as Figure 3 for x=3.0L.

Figure 5.   Current density vectors in the y-z plane at x=3.0L at $T=14.6\tau_A$. Superimposed on the current density vectors are contours of magnetic field magnitude.

Figure 6.   The field aligned current density contours in Figure 4 (shaded region) have been superimposed on the current density vectors and magnetic field contours of Figure 5. The numbers refer to values of the field aligned current density normalized to the initial neutral sheet current.

Figure 7.   Velocity along the x-axis at $T=14.6\tau_A$. Reconnection is occurring at x=0. The magnetosonic velocity is given by V_f.

Figure 8.   The cross tail current density along the x-axis at $T=14.6\tau_A$.

Figure 9.   The pressure and reconnected field along the x-axis at $T=14.6\tau_A$.

Figure 10.   Power through the three boundaries of the simulation box. 1, 2 and 3 give the kinetic power through the output (x=3L), side (y=5L) and input (z=2L) boundaries. 4, 5 and 6 give the thermal power through the boundaries while 7, 8 and 9 give the magnetic power through the boundaries.

Figure 11.   Flow vectors in the y-z plane at x=0 at $T=14.6\tau_A$.

Figure 12. Work done within the simulation box. $\int (J \times B) \cdot v\,dV$ gives the work done by the $\underline{J} \times \underline{B}$ force, $\int \nabla P \cdot v\,dV$ gives the work done by the pressure force and $\int \eta J^2\,dv$ gives the work done by the Joule heating.

Figure 13. Total kinetic ($\int \rho\, v^2\,dV$), thermal ($\int \frac{P}{\gamma-1}\,dV$) and magnetic ($\int \frac{B^2}{2\mu_0}\,dV$) energies versus time.
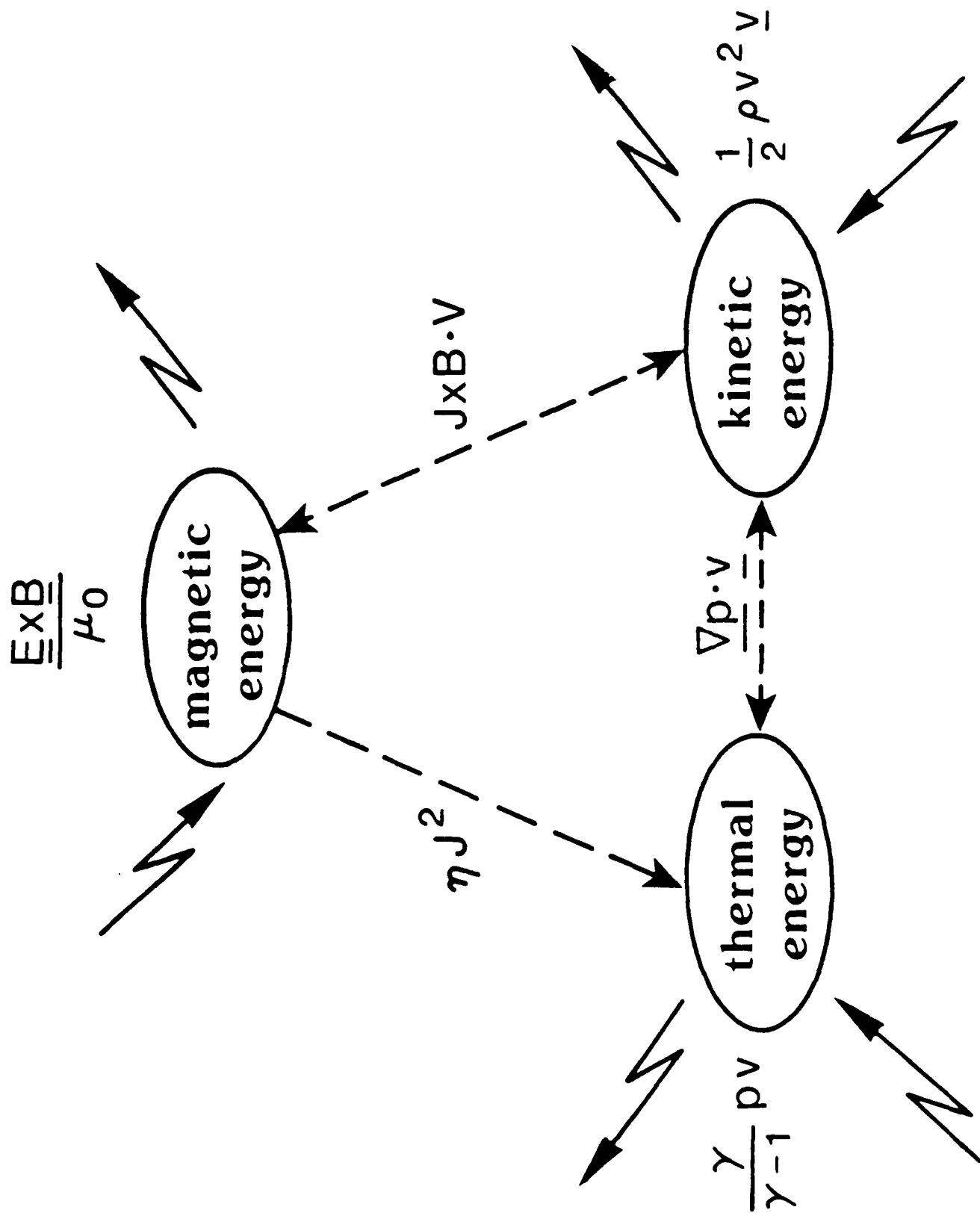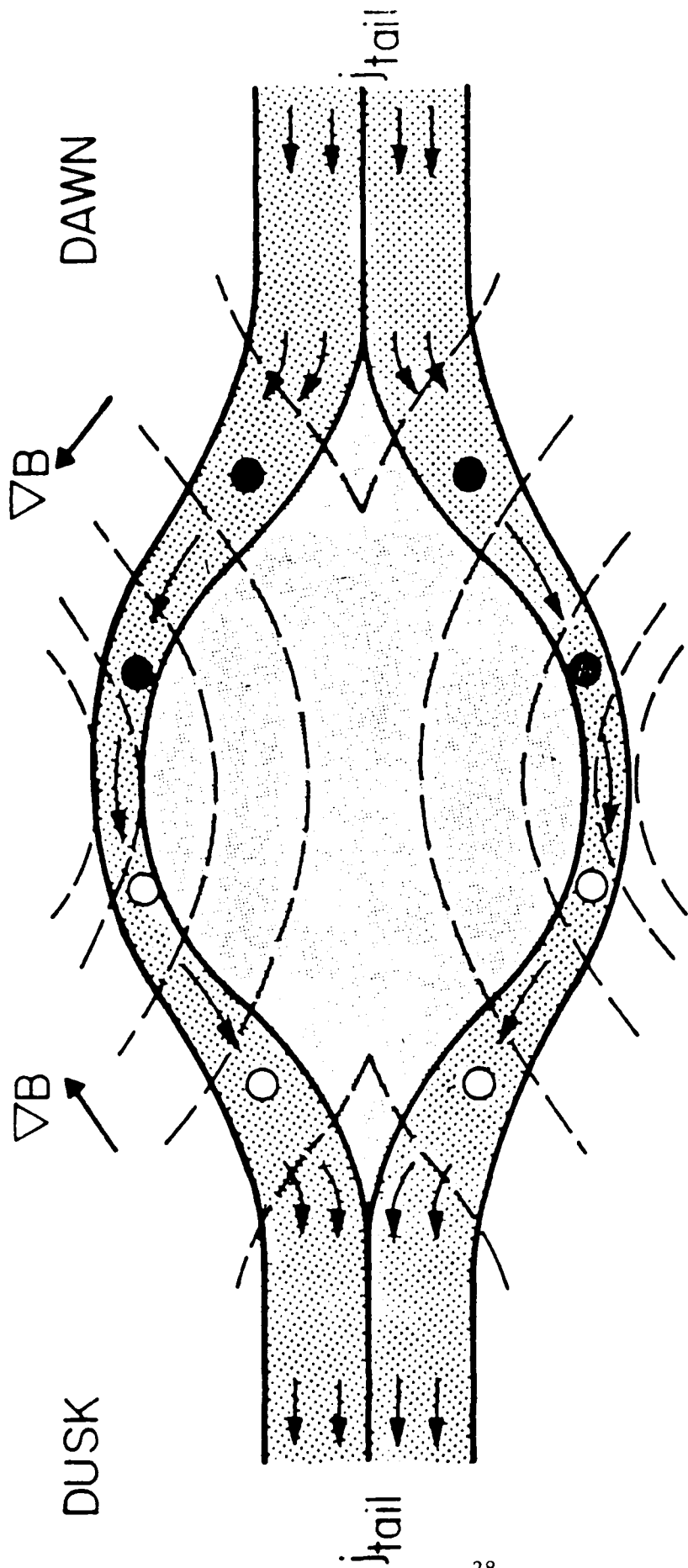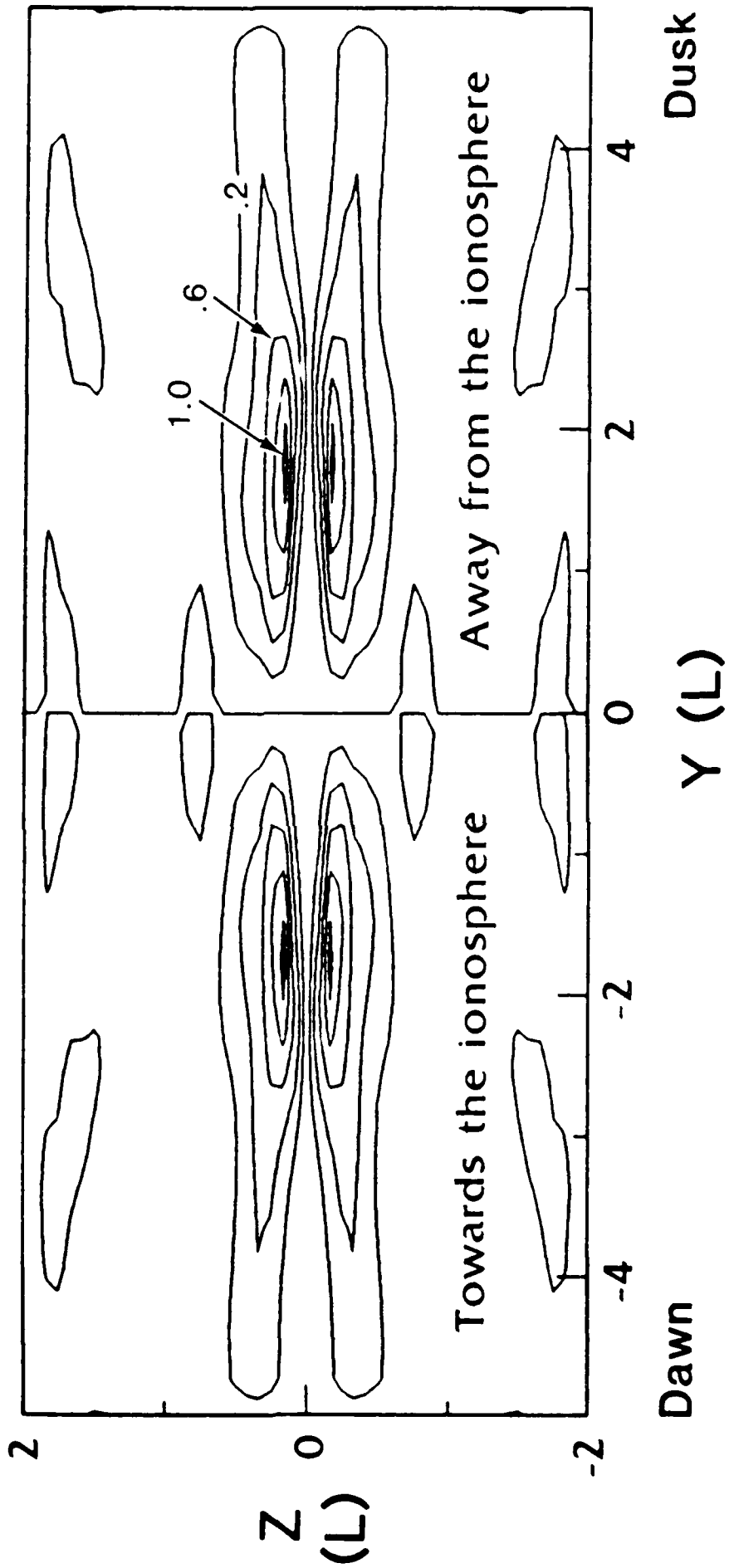
Fig. 1

DUSK

DAWN

j_{tail}

j_{tail}

∇B

∇B

○ $j_{\parallel}$ AWAY FROM THE EARTH

● $j_{\parallel}$ TOWARD THE EARTH

Fig. 2

28

FIELD ALIGNED CURRENT DENSITY
$(X = 2.25L, T = 14.6\tau_A)$

Towards the ionosphere

Away from the ionosphere

Dawn

Dusk

Y (L)

Z (L)

Fig. 1

FIELD ALIGNED CURRENT DENSITY

$(X = 3.0\,L,\ T = 14.6\ \tau_A)$
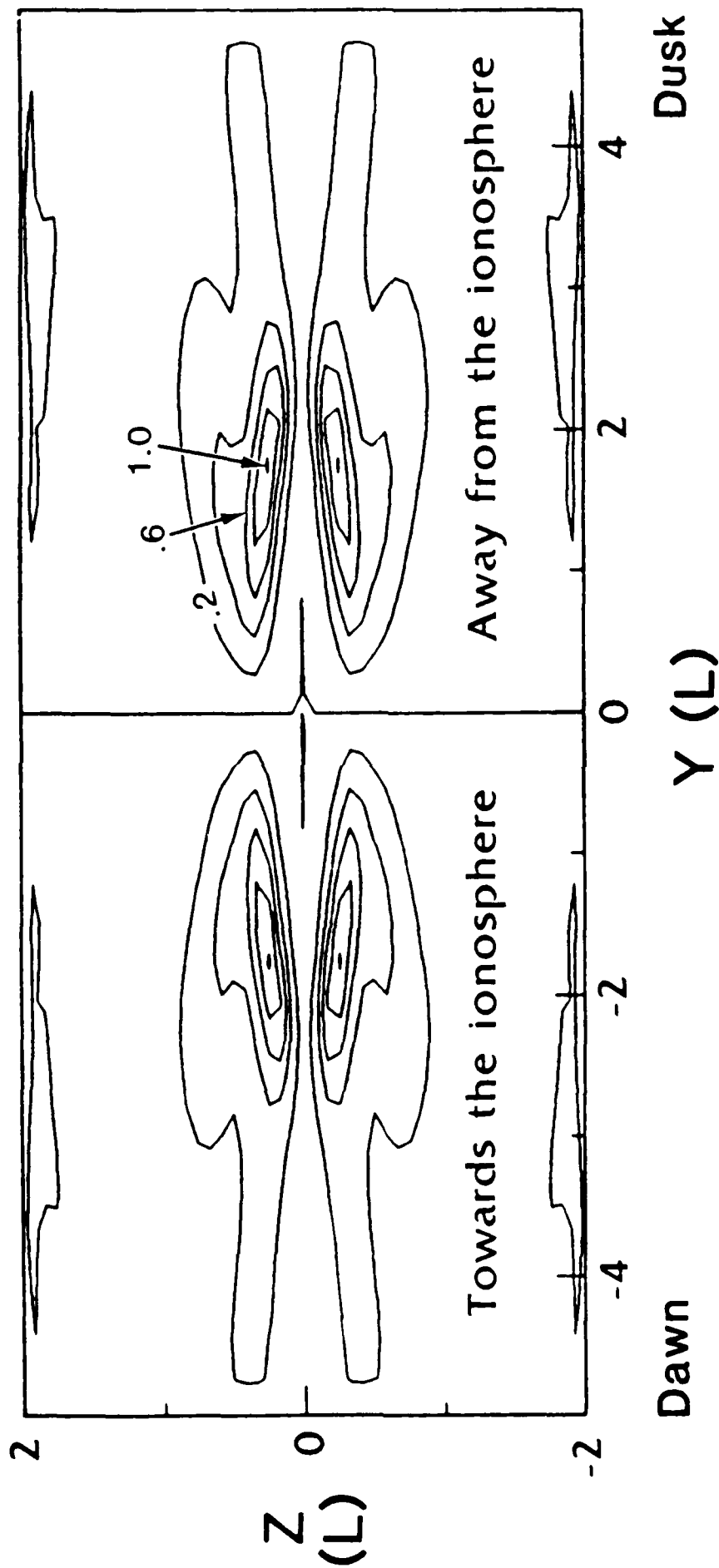
Dusk

Away from the ionosphere

1.0

.6

.2

Y (L)

Towards the ionosphere

Dawn

Z (L)

Fig. 4

30

CURRENT DENSITY AND IBI

$(X = 3.0L, T = 14.6 \tau_A)$

Dusk

Dawn

Y (L)

Z (L)

CURRENT DENSITY AND IBI

$(X = 3.0L, T = 14.6 \tau_A)$

Fig. 6

Figure axis labels:
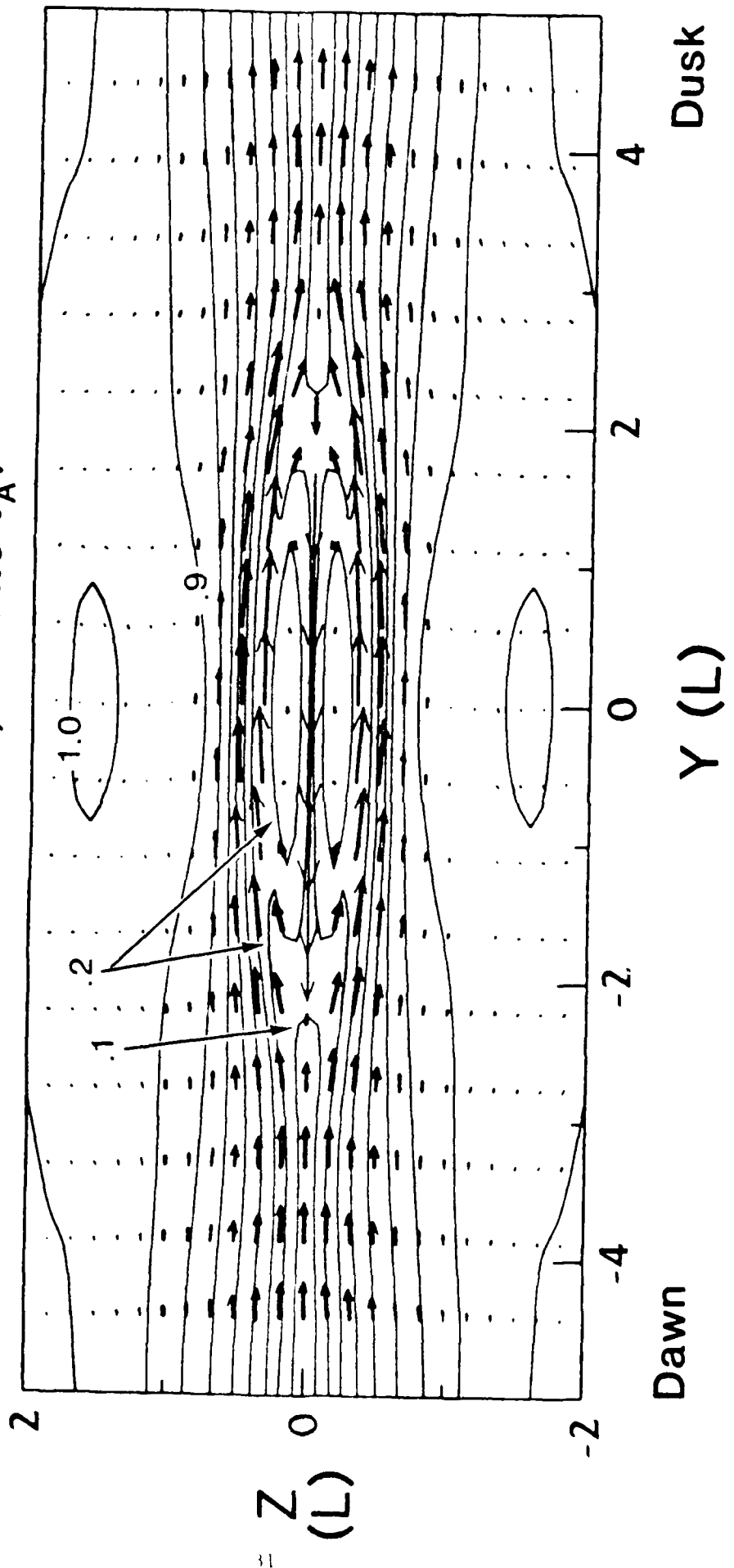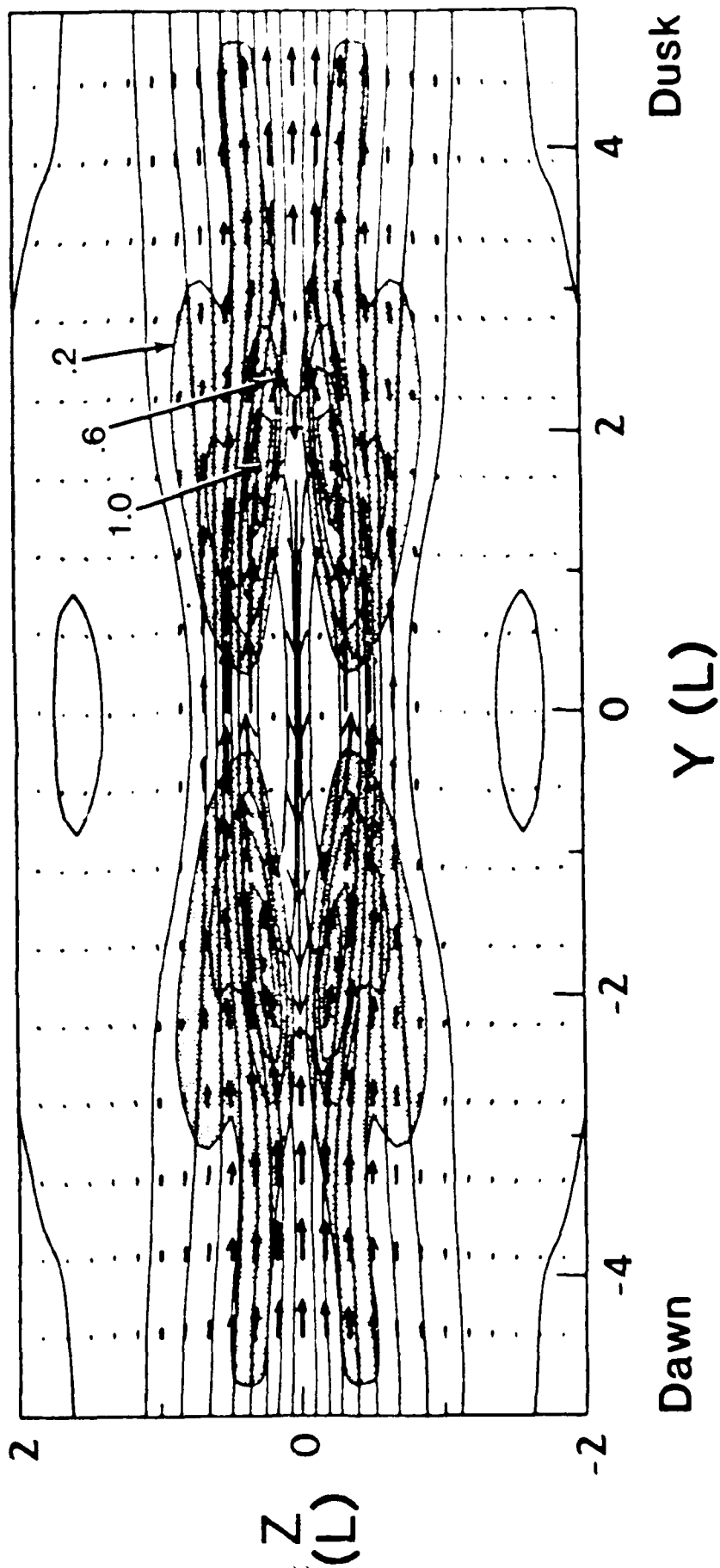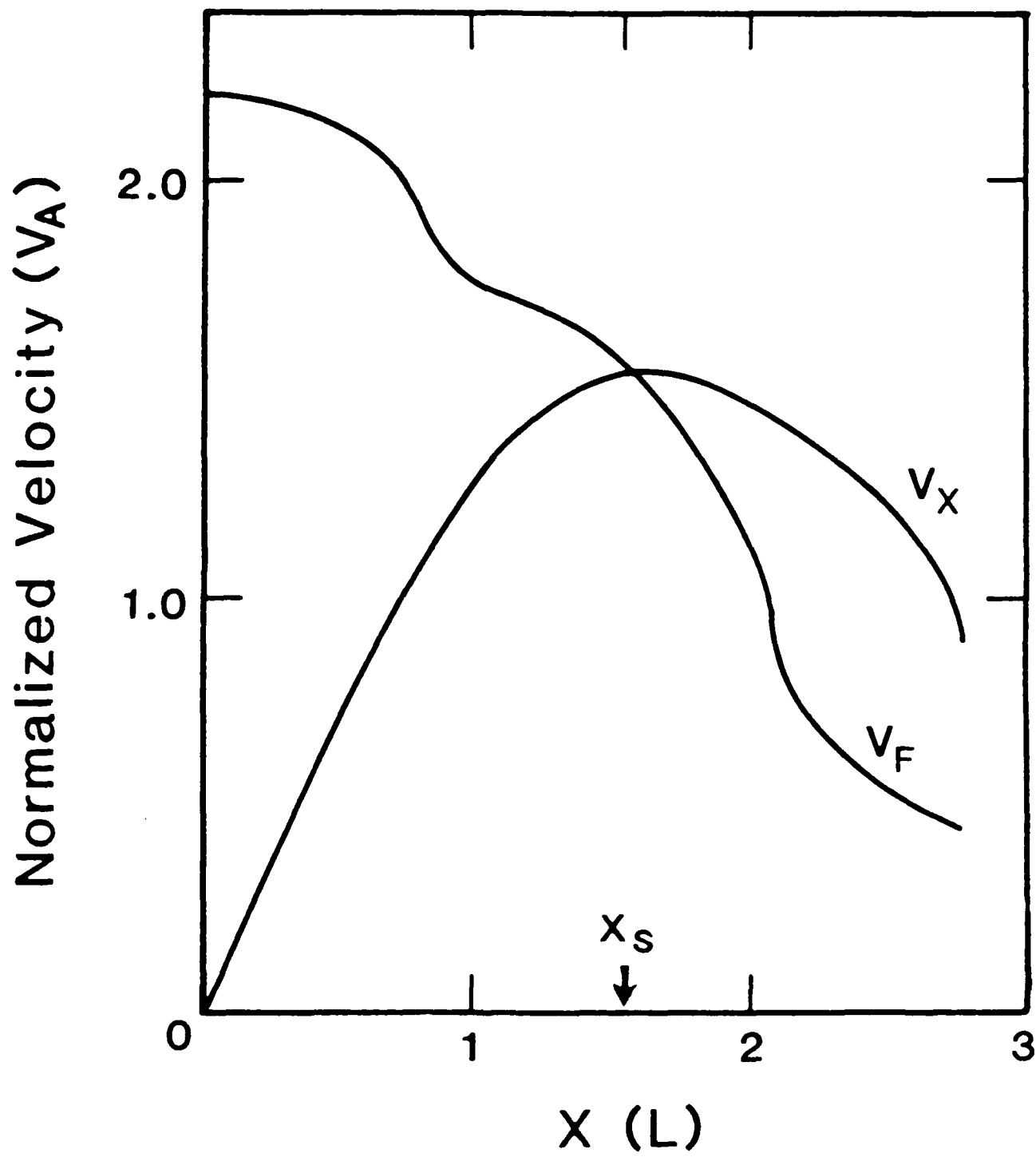
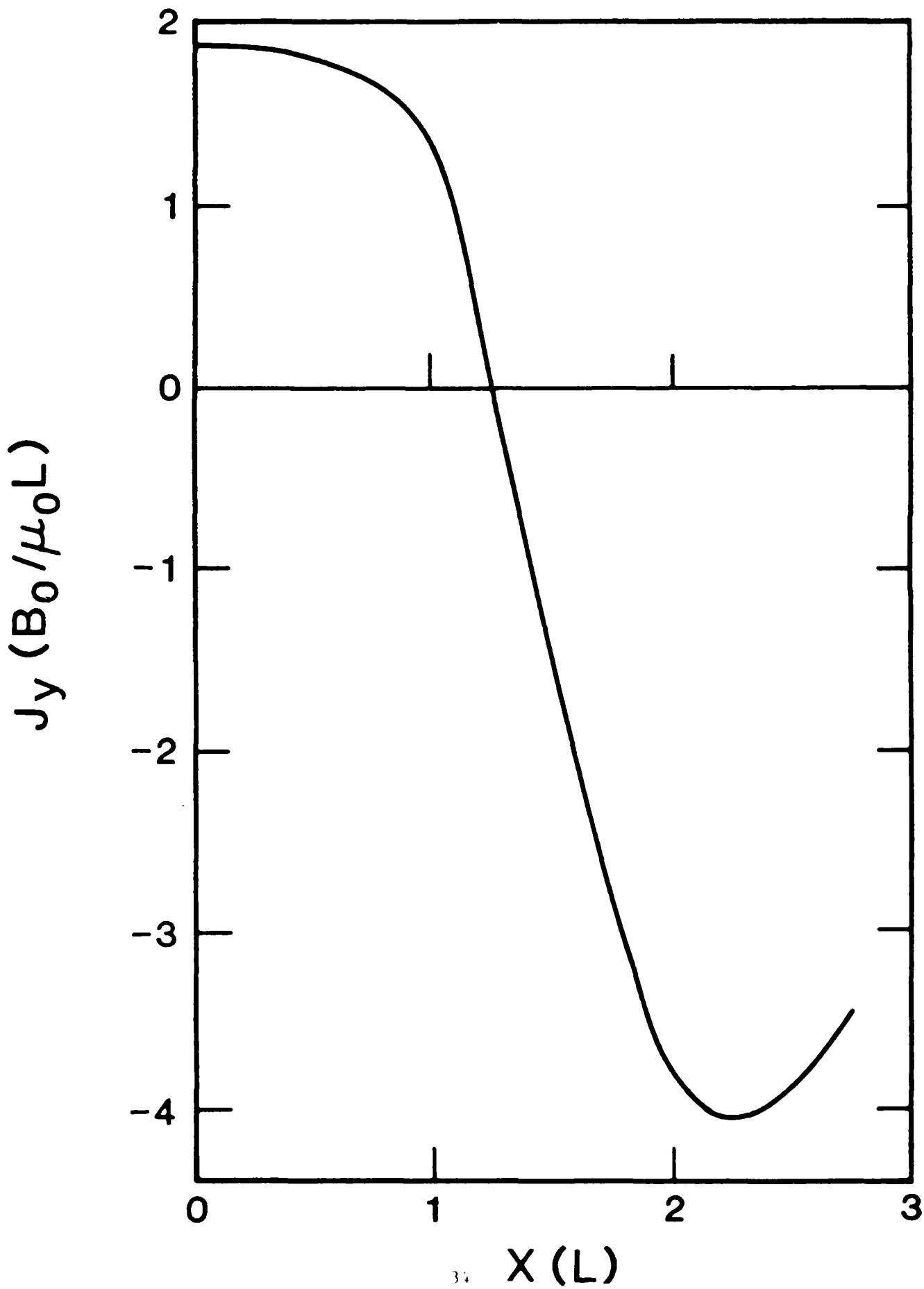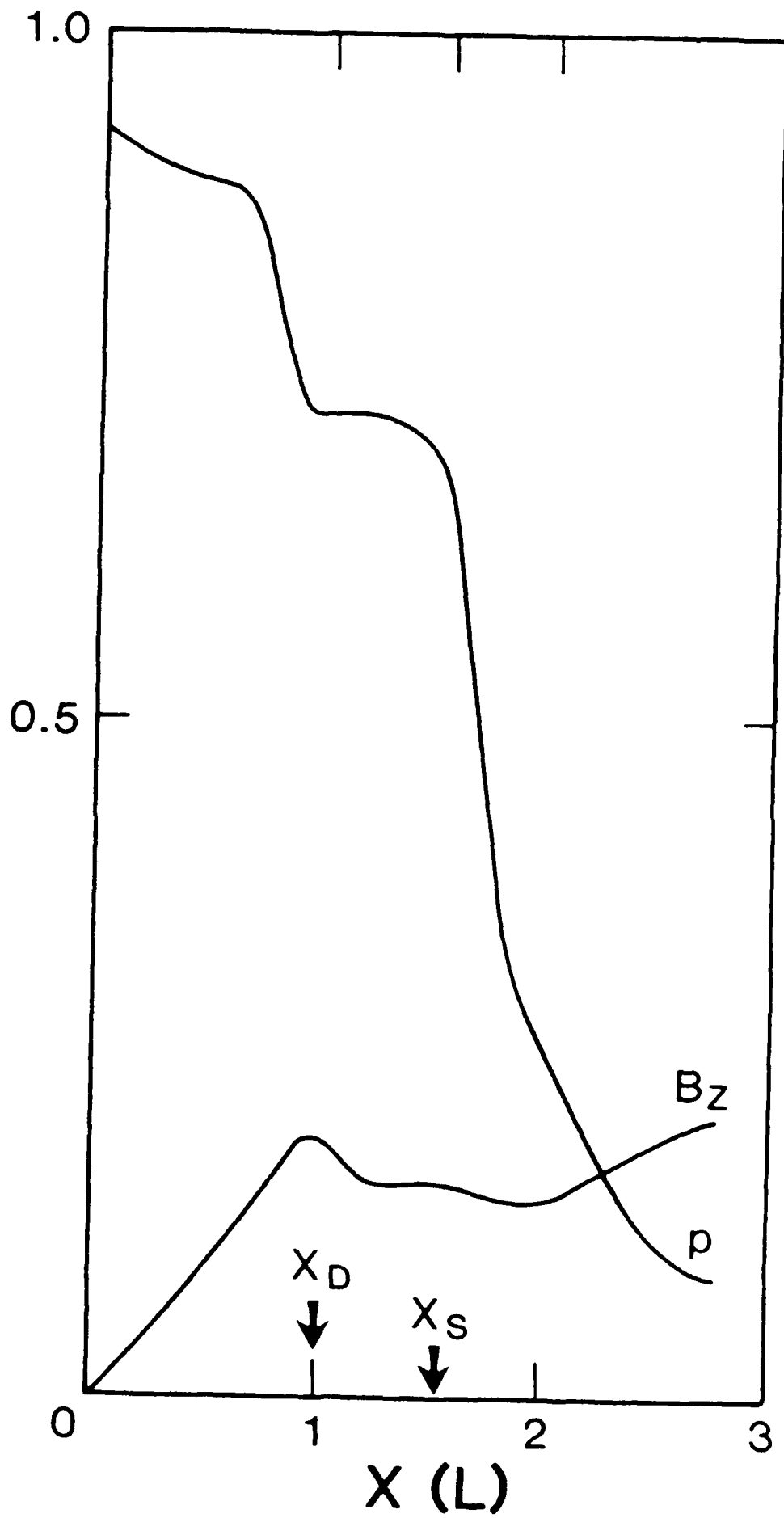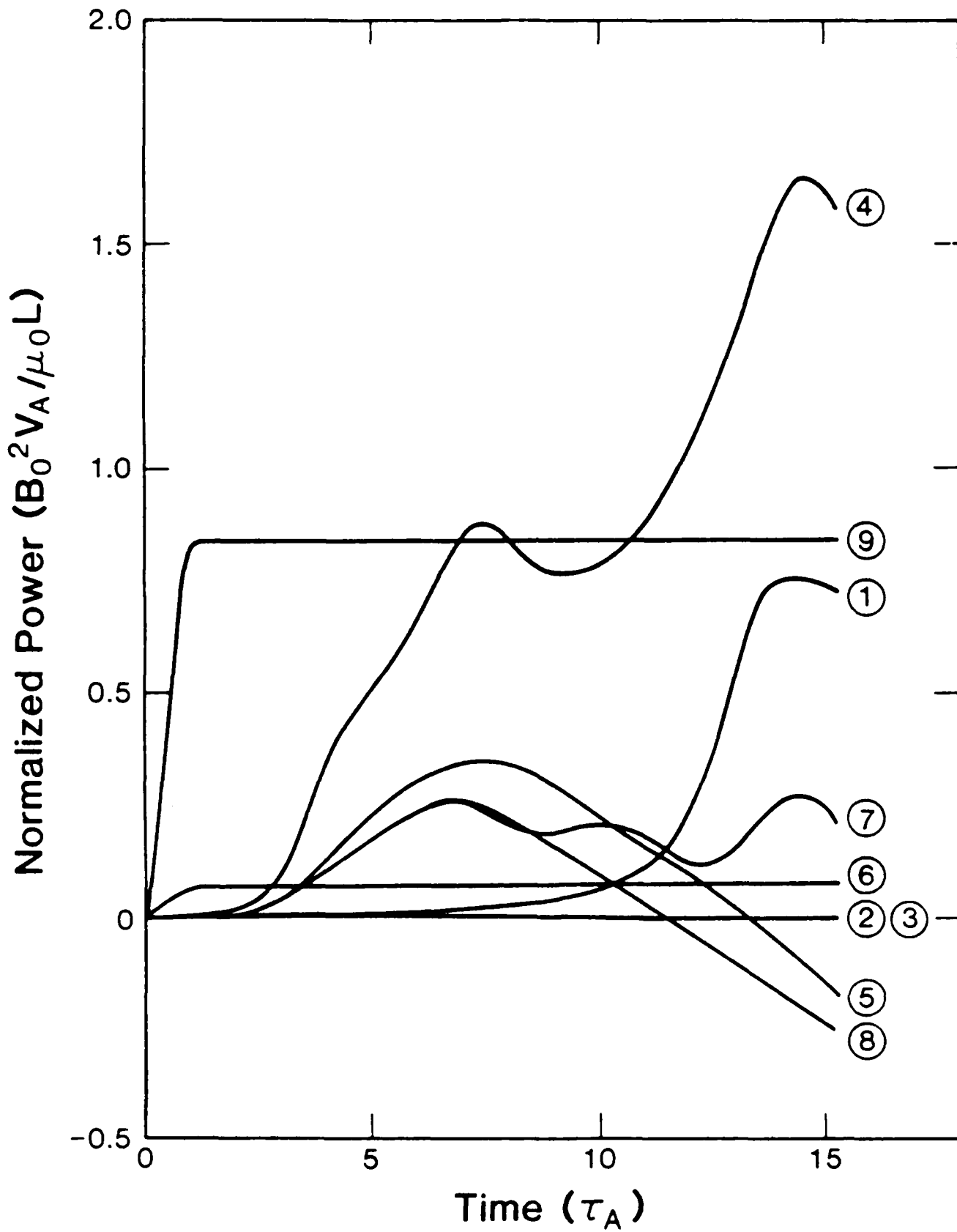Y-axis: Normalized Units ($p = B_0^2/2\mu_0$, $B = B_0$)

Values: 1.0, 0.5, 0

Curves labeled: B_Z, p

X-axis markers: X_D, X_S

X-axis: X (L), values 0, 1, 2, 3

35

Fig.

Flow $(X = 0, T = 14.6\ \tau_A)$

The figure plots Normalized Power $(B_0^2 V_A/\mu_0 L)$ versus Time (τ_A), showing curves labeled $\int (j \times B) \cdot v\, dV$, $\int \nabla p \cdot v\, dV$, and $\int \eta j^2\, dV$.

38

Fig. 12

Fig. 13

39
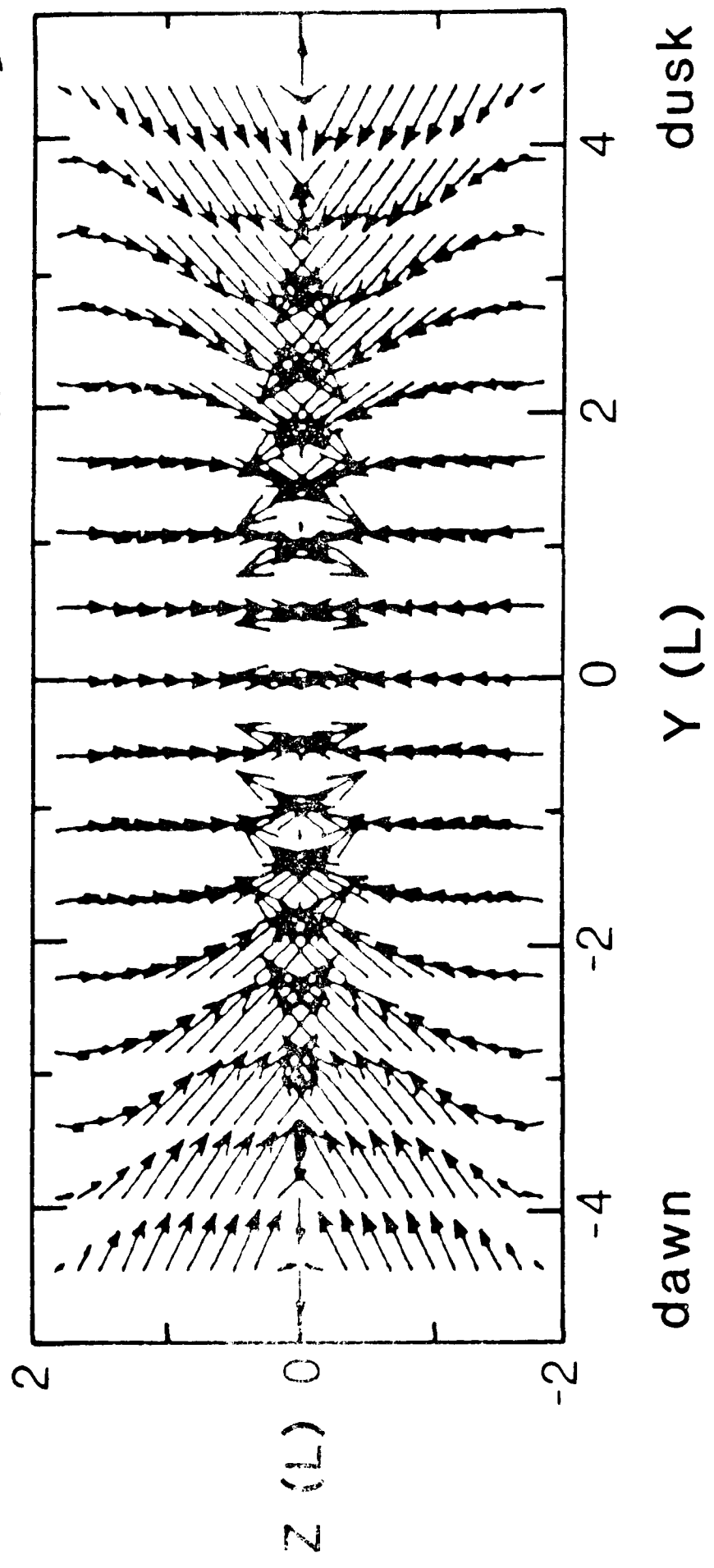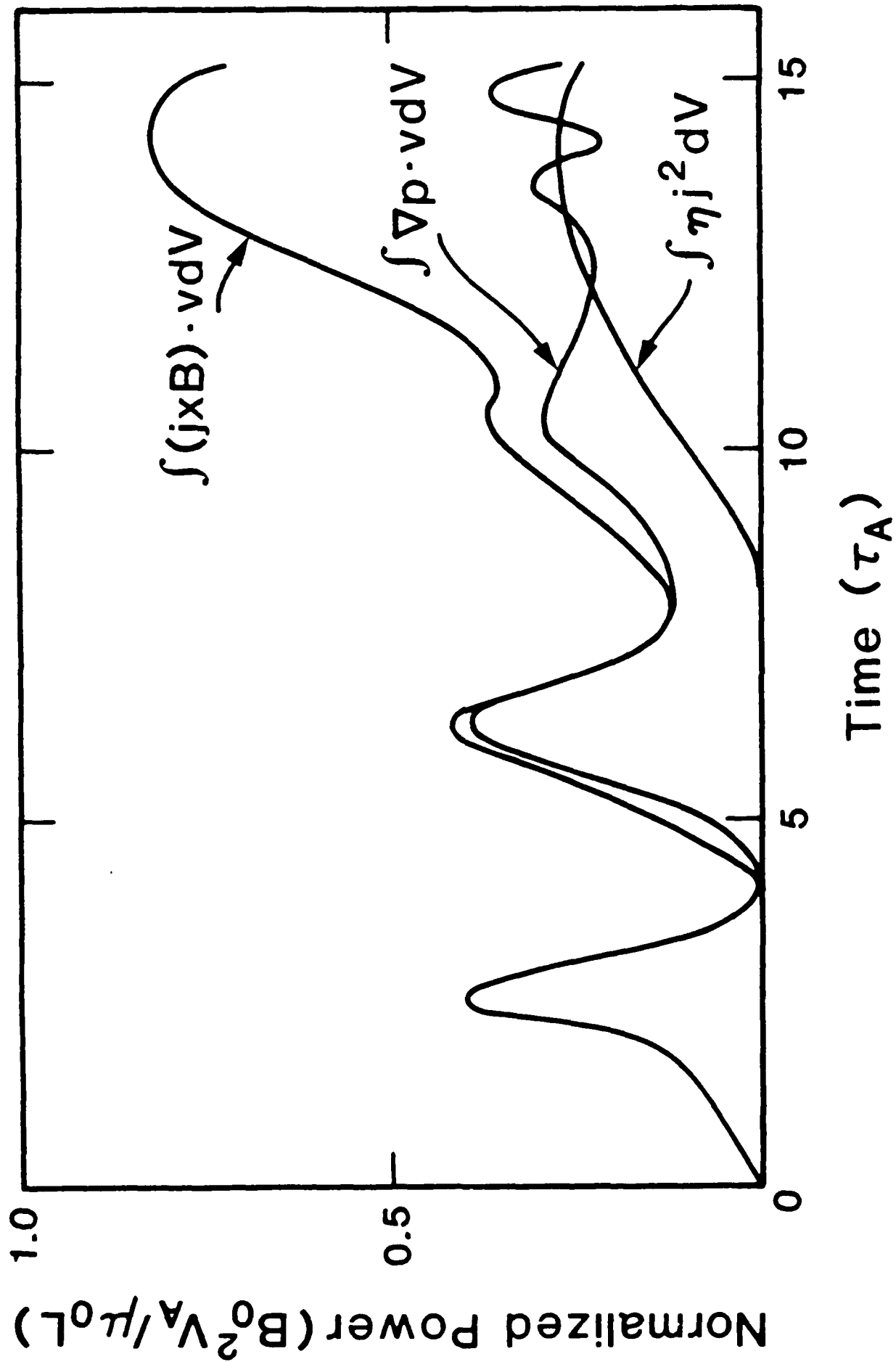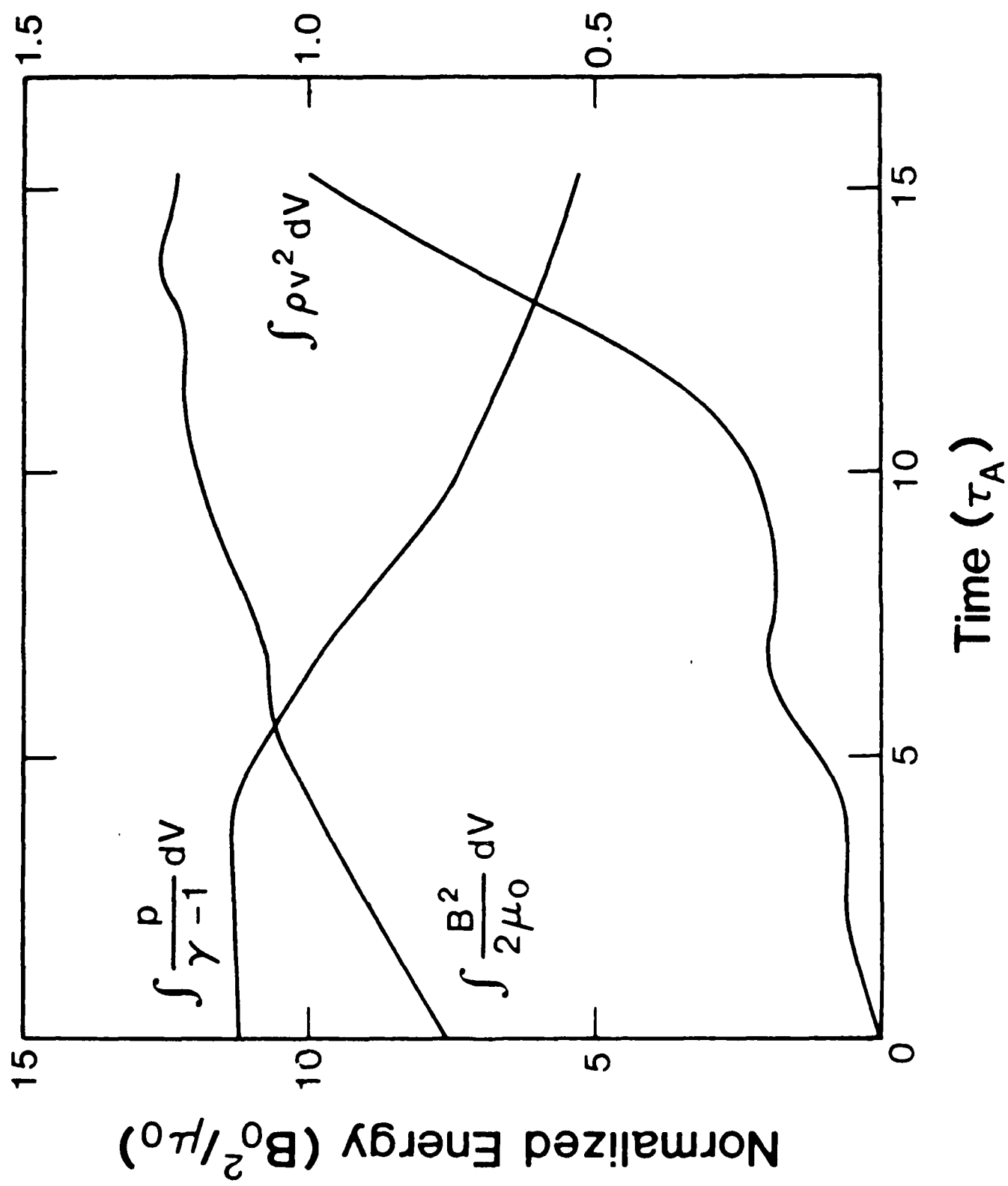
References

Akasofu, S.-I., Interplanetary energy flux associated with magnetospheric sub-
storms, Planet. Space Sci., 27, 425, 1979.

Akasofu, S.-I., The solar wind-magnetosphere energy coupling and magnetospheric
disturbances, Planet. Space Sci., 28, 495, 1980.

Birn, J. and E.W. Hones, Jr., Three-dimensional computer modeling of dynamic
reconnection in the geomagnetic tail, J. Geophys. Res., 86, 9, 6802, 1981.

Brecht, S.H., J.G. Lyon, J.A. Fedder, and K. Hain, A time-dependent three-dimen-
sional simulation of the Earth's magnetosphere: Reconnection events,
J. Geophys. Res., 87, A8, 6098, 1982.

Hasegawa, A. and T. Sato, Generation of field-aligned currents during substorms,
in Dyanamics of the Magnetosphere, edited by S.-I. Akasofu, D. Reidel
Publ. Co., Boston, 529p., 1979.

Hayashi, T. and T. Sato, Magnetic reconnection: Acceleration, heating, and
shock formation, J. Geophys. Res., 83, 217, 1978.

Hones, E.W., Jr., Plasma flow in the plasma sheet and its relation to substorms,
Radio Sci., 8, 979, 1973.

Leboeuf, J.N., T. Tajima, C.F. Kennel, and J.M. Dawson, Global simulations of
the three-dimensional magnetosphere, Geophys. Res. Lett., 8, 3, 257, 1981.

McPherron, R.L., C.T. Russell, and M.P. Aubry, Satellite studies of magneto-
spheric substorm on August 15, 1968, 9. Phenomenological model of sub-
storms, J. Geophys. Res., 78, 3131, 1973.

Perreault, P. and S.-I. Akasofu, A study of geomagnetic storms, J. R. Astr.
Soc., 54, 547, 1978.

Petschek, H.E., Magnetic field annihilation, NASA Spec. Publ., SP-50, 425, 1964.

Russell, C.T. and McPherron, R.L., The magnetotail and substorms, Space Sci.
Rev., 15, 205, 1973.

Sato, T., Strong plasma acceleration by slow shocks resulting from magnetic reconnection, J. Geophys. Res., 84, A12, 7177, 1979.

Sato, T. and T. Hayashi, Externally driven magnetic reconnection and a powerful magnetic energy converter, Phys. Fluids, 22, 1189, 1979.

Sato, T., Auroral physics, in Magnetospheric plasma physics, edited by A. Nishida, Center for Academic Publ., Japan and D. Reidel Publ. Co., Tokyo, Japan, 1982.

Sato, T. and T. Iijima, Primary sources of large-scale Birkeland currents, Space Sci. Rev., 24, 307, 1979.

Sato, T. and T. Hayashi, Three-dimensional simulation of spheromak creation and disruption, Institute for Fusion Theory, Hiroshima University, preprint HIFT-66, 1982.

Sato, T., T. Hayashi, T. Tamao, and A. Hasegawa, Confinement and jetting of plasmas by magnetic reconnection, Phys. Rev. Lett., 41, 1548, 1978.

Sato, T., T. Hayashi, R.J. Walker, and M. Ashour-Abdalla, Neutral sheet current interruption and field aligned current generation by three-dimensional driven reconnection, Geophy. Res. Lett., 10, 3, 221, 1983.

Vasyliunas, V.M., Theoretical models of magnetic field line merging, 1, Rev. Geophys. Space Phys., 13, 303, 1975.

Vasyliunas, V.M., Fundamentals of current description, magnetospheric currents, T.A. Potemra, ed., Geophys. Monograph, 28, 63, 1984.

Walker, R.J. and T. Sato, Driven magnetic reconnection, E.W. Hones, Jr., ed., Magnetic Reconnection in Space and Laboratory Plasmas, Geophys. Monograph, 30, 272, 1984.

Wu, C.C., Shape of the Magnetosphere, Geophys. Res. Lett., 10, 7, 545, 1983.

Heating of Thermal Helium

in the Equatorial Magnetosphere :

a Simulation Study

Y. Omura[1]

M. Ashour-Abdalla

K. Quest[2]

R. Gendrin[3]

Institute of Geophysics and Planetary Physics

University of California, Los Angeles, CA 90024

November, 1984

[1]Radio Atmospheric Science Center

Kyoto University, Uji, Kyoto 611, Japan

[2]Los Alamos National Laboratory, Los Alamos, NM 98545

[3]Centre de Recherches en Physique de L'Environnement,

Centre National d'Etudes des Telecommunications,

3 Avenue de la Republique, 92131, Issy-les-moulineaux, France

Acknowledgements

Abstract

One of the challenging magnetospheric plasma physics problem is the heating of heavy ions observed in the equatorial magnetosphere in conjunction with ion cyclotron waves (ICW) generated by anisotropic hot protons (i.e., GEOS-1 and 2 and ATS 6 results). The complexity of the mechanisms involved in this phenomenon (linear, quasi-linear, nonlinear) is such that a numerical simulation is the only way to disentangle the different plasma characteristics. We present here the results of such a simulation. The plasma parameters which have been chosen are those which prevail in the dayside magnetosphere at geostationary altitudes. The plasma consists of cold and isotropic H^+ and He^+ ions with a small number of hot anisotropic protons which provide the free energy necessary to generate the waves. The code is one-dimensional in length and three-dimensional in velocity. It is electromagnetic and hybrid, i.e., the electrons are treated as a massless fluid. The results obtained during the linear phase ($t \leqslant 150 \, \Omega_H^{-1}$) are in agreement with those expected from the linear and quasi-linear theories as far as the growth rate of the wave (and the frequency of the most amplified wave) and the variation of the hot proton anisotropy are concerned. The saturation ($B_{wave} \sim 0.05 \, B_0$) is explained by trapping of the helium particles. But the most interesting results concern the heating of cold species. He^+ ions are heated mainly in the perpendicular direction ($kT_\perp/2 \simeq 150$ eV, $kT_\parallel/2 \simeq 80$ eV) and they are heated more than cold H^+ ions ($kT_\perp/2 \simeq 15$ eV, $kT_\parallel/2 \simeq 20$ eV). The heating of He^+ ions is a two-step process : first, He^+ ions are set into oscillations by the growing wave (in both $v_\perp$ and $v_\parallel$) until some of the ions reach a parallel velocity of the order of the resonant velocity at which time strong heating occurs. Phase-space plots for the different particle species at different times illustrate the time evolution of this heating mechanism.

47

I Introduction

It has recently been recognized that heavy ions are important to the dynamics and stability of different regions in the earth's magnetosphere. Shelley et al. [1976] and Ghielmetti et al. [1978] have reported observations of intense fluxes of O^+ streaming up high-latitude auroral field lines at altitudes of ~ 1 R_E. Data from the S3-3 satellite show that ion composition can vary from 10% to more than 90% oxygen [Mizera et al.. 1980].

The inferences of O^+ streams deep in the magnetotail boundary layer by Frank et al. [1977] and Hardy et al. [1977] suggest that there might be measurable fluxes of energetic O^+ ions of terrestrial origin deep in the plasmasheet. Results from the energetic ions mass spectrometer on ISEE-1 show that the plasmasheet has a significant and variable ionospheric component (He^+ and O^+) which represents from more that 10% to 50% of the total number density [Petersen et al.. 1981].

At the geostationary orbit. O^+ and He^+ ions of medium energy (~ 10 keV) have been found to be important constituents of magnetospheric plasma. especially during magnetic storms [Geiss et at.. 1978; Young. 1979; Balsiger et al.. 1980]. But the most intriguing result is the observations. made onboard GEOS-1 and -2 and ATS-6 spacecrafts that He^+ or O^+ ions are heated up to suprathermal energies (~ 100 eV) at times when large amplitude ions cyclotron waves (ICW's) are detected [Young et al.. 1981; Mauk et al.. 1981; Roux et al.. 1982; Fraser. 1982].

The facts that heavy ions occur in many different regions of the magnetosphere. that they are of terrestrial origin and that they can be a major constituent of the plasma motivated the community to reexamine theoretical studies of wave particle interactions including the effects of heavy ions. When studying wave particle interactions in the presence of heavy ions there are two problems that should be addressed. The first is the effect of the heavy ions on the dynamics and stability of a plasma.

49

The second and more pertinent problem is to understand the mechanism responsible for energizing such heavy ions.

Several studies have addressed these questions for different regions of the magnetosphere. On auroral field lines, the heating of O^+ has been studied by using electrostatic waves [Lysak et al., 1980; Papadopoulos et al., 1980; Ashour-Abdalla et al., 1981; Ashour-Abdalla and Okuda, 1984]. Lysak et al. [1980] used strong turbulence theory, which considered the ion orbits in a set of fixed amplitude waves with a definite phase relation. Papadopoulos et al. [1980] argued that the heavy ions form a minority constituent of many magnetospheric multi-ion plasmas. As such, the heavy ions do not affect the collective mode structure of the plasma due to their small abundance ratios. They thus examined the acceleration of large M/Q ions in the presence of a coherent large amplitude electrostatic hydrogen cyclotron wave. It was found that when the wave amplitude exceeds a certain critical value the particle orbits become stochastic and the particles can be accelerated by the wave. The most important result was that the maximum energy achieved by an ion scales as $(M/M_H)^{5/3}$, where M_H is the mass of hydrogen and M is the mass of the ion under consideration. They concluded that heavy ions are thus preferentially accelerated. Ashour-Abdalla and Okuda [1984] studied the acceleration of ions on auroral field lines associated with the current-driven electrostatic ion cyclotron waves in a plasma consisting of hydrogen and oxygen ions by simulation techniques. To model the ionospheric source of electrons they developed a simulation model in which drifting electrons were allowed to enter at the end of the system. They found that the oxygen transverse heating generally exceeds that of hydrogen ions at the low altitude end of the field line.

There have also been studies using electromagnetic waves to explain the acceleration of heavy ions. Theoretically it is well known that the presence of heavy ions greatly modifies the propagation and amplification characteristics of magnetospheric electromagnetic waves. A detailed

50

analysis of the wave spectra and energetic proton distribution measured on GEOS-1 have shown that the observed wave spectra can be interpreted in the framework of the linear theory of ion cyclotron instability excited by an anisotropic proton distribution in a plasma containing a small fraction ~5 -15% of He^+ ions [Roux et al.. 1982]. Gomberoff and Cuperman [1982] have also performed a theoretical analysis in order to evaluate the change in the temporal growth rate of such instabilities for various plasma parameters. Gomberoff and Neira [1983] undertook the task of evaluating the corresponding change in the spatial growth rate. However. such studies have generally been done assuming the background plasma to be completely cold. $T(H^+) = T(He+) = 0$. whereas it is known from GEOS and DE experiments that both electrons and ions can reach a temperature equal to or higher than 10 eV [Decreau et al.. 1982; Chappell. 1983]. Under such conditions. cyclotron absorption by the heavy ion species will compete with the amplification induced by hot protons. and growth rates will be strongly modified. especially in the vicinity of the heavy ion gyrofrequency. Recently Gendrin et al. [1984] carried out a parameter search of ion cyclotron waves including the finite temperature effects associated with the cold species.

The heating of heavy ions by electromagnetic ion cyclotron waves has been addressed by several authors. Gendrin and Roux [1980] have studied the possibility that the observed heating of He^+ ions up to suprathermal energies could be explained by quasi-linear diffusion. Indeed quasi-linear diffusion of resonant He^+ ions having low initial parallel and perpendicular velocities can lead to a considerable increase of the perpendicular He^+ ion distribution. However. to heat the bulk of He^+ distribution. sufficient wave energy must be available at frequencies where a resonant interaction with the cold heavy ion species can take place. i.e.. at frequencies which are near the heavy ion gyrofrequency. Gendrin et al. [1984] found that the maximum growth rates occur at frequencies far

from the heavy ion gyrofrequency; consequently these waves cannot resonate with the bulk of heavy ion distribution. In search of another heating mechanism, Mauk [1982, 1983] studied the nonresonant interaction between an electromagnetic ion cyclotron wave and thermal He$^+$ ions. He showed that associated with the increase in the He$^+$ ion perpendicular velocity, phase bunching was observed. Unfortunately, Mauk's calculations were done by neglecting the ion parallel velocity, which led to incorrect quantitative results: an apparently infinite increase of $v_\perp$ as time elapses and a strong effect even when the wave frequency is equal to the helium cyclotron frequency. Berchem et al., [1983] and Berchem and Gendrin [1984] extended Mauk's work to include the parallel velocity of the ions. They found that phase bunching occurs, and the particle attains large perpendicular velocities. They carried out a parameter search as a function of initial parameters and were able to derive approximate analytical expressions for the maximum temperature of the heavy ions attained. These calculations were test particle calculations in which the wave amplitude was kept constant, and were therefore not self-consistent. In search of self-consistency, Tanaka and Goodrich [1984] used simulation techniques to study the heating of heavy ions at different regions of the magnetosphere with particular emphasis on the heating of Alpha particles at the bow shock. As such they considered a plasma consisting of hot highly anisotropic protons in the presence of a minority species. Since these studies were concerned with gaining an understanding of He^{++} at the shock region, they did not include a cold hydrogen background representative of the ionospheric source.

For sake of completeness, it is worth mentioning that a similar mechanism (resonant interaction of one ion species with waves generated by a majority ion) has been invoked to explain the excess of He^{++} ion bulk velocity in the solar wind. However, it is only until recently that the fundamental modification brought in to the dispersion relation by the

presence of the heavy ions has been correctly taken into account. which means that the results previously obtained are not relevant to the problem we are studying here (see Isenberg, [1984a,b] and references therein).

In this paper, our aim is to explain the heating of He^+ observed by the GEOS satellite at L ~ 7. Our starting points is the observation set from the GEOS satellite. Having developed the linear theory analysis in a recent paper [Gendrin et al., 1984]. we undertake a simulation study of electromagnetic ion cyclotron waves in a plasma consisting of hot anisotropic protons, a dominant thermal hydrogen plasma, and a minority species of helium ions. Following this introduction, in section II the computational model is described. simulation results of our three ion component plasma are presented in section III. We conclude in section IV by summarizing and discussing the pertinent heating mechanisms.

II Simulation Model

We have developed a one dimensional electromagnetic hybrid simulation code [Sgro and Nielson, 1976; Byers et al., 1978] where electrons are treated as a massless fluid and ions are treated as particles moving in the four dimensional phase space (x, v_x, v_y, v_z). Since we are studying low frequency phenomena, we neglect the transverse displacement current in Maxwell's equations (Darwin approximation) as

$$\frac{\partial B}{\partial t} = - \text{rot } E \tag{1}$$

$$\mu_o J = \text{rot } B \quad . \tag{2}$$

We also neglect electron inertia effects for low frequency waves, and we have from the electron momentum equation

$$-en_e(E + u_e \times B) - \text{grad } p_e = 0 \tag{3}$$

where $-e$, n_e, u_e and p_e are electron charge, number density, flow velocity and pressure, respectively. Furthermore, we assume the quasi-neutrality condition

$$-en_e + q_s n_s = 0 \tag{4}$$

where q_s and n_s are the charge and number density of an "s" ion species, respectively. The electron pressure is integrated in time by using the electron energy equation

$$\left(\frac{\partial}{\partial t} + u_e \cdot \text{grad}\right) p_e = - \frac{5}{3} p_e \text{ div } u_e \quad . \tag{5}$$

The electron flow u_e is obtained from the current equation as

$$u_e = (\Sigma q_s n_s u_s - J)/n_e q_e \tag{6}$$

where U_s is the drift velocity of a "s" ion species. The ion density n_s and drift velocity u_s are calculated from the motion of ion particles whose positions and velocities are determined by integrating the equations of motion

$$\frac{dv}{dt} = \frac{q_s}{m_s} (E + v \times B), \qquad \frac{dx}{dt} = v \qquad . \qquad (7)$$

The magnetic field B and the electron pressure p_e are integrated in time using (1) and (5), while the electric field is determined by a predictor-corrector method using (2), (3), (4) and (6).

For simplicity, spatial variations are restricted to one dimension, i.e., the x direction, and periodic boundary conditions are assumed. We focus our attention on waves propagating parallel to the external magnetic field. Therefore, both the wave vector k and the static magnetic field B_0 are in the x direction. We consider three species of ions, i.e., cold H^+, cold He^+ and hot H^+ with bi-Maxwellian velocity distribution. Initially both cold components are isotropic and hot protons have a temperature anisotropy of $T_\perp/T_\parallel = 2$. These particles are distributed uniformly over the simulation space consisting of 64 grid points. No wave field is assumed initially except for noises introduced by particle thermal fluctuations.

The parameters of the simulation have been chosen to represent typical conditions prevailing during the day hours at the geostationary orbit where most of events involving ICW's and energized He^+ ions have been observed:

- magnetic field intensity : 140 nT.
- cold H^+ ion density 10 cm^{-3}.
- cold He^+ ion density : 2 cm^{-3}.
- thermal energy of both cold species : 1.7eV.
- anisotropy of both cold species : $T_\perp/T_\parallel = 1$.
- hot proton density : 1.1 cm^{-3}.
- thermal parallel energy of hot protons : 17 keV.
- anisotropy of hot protons : $T_\perp/T_\parallel = 2$.

Note that with these parameter the ratio of the ion plasma frequency ω_H to the proton gyrofrequency Ω_H is equal to 300, and that the Alfven energy $mV_A^2/2 \sim 5$ keV, so that the parallel β of the plasma is ~ 0.3.

55

In the simulation we do not use the physical parameters as expressed in CGS or MKS units, but instead use conventional normalizations. It is simpler to use a system in which the Alfven velocity V_A, the proton cyclotron frequency Ω_H, the proton charge-to-mass ratio $(q/m)_H$ and the magnetic permeability μ_0 are equal 1. Other parameters are normalized to the quantities stated above. Since the static magnetic field is given by $B_0 = \Omega_H/(q/m)_H$, $B_0 = 1$ and the static magnetic energy density $B_0^2/2\mu_0 = 0.5$. The light speed c is equal to $V_A(\omega_H/\Omega_H) = 300$, from which the electric permittivity $\varepsilon_0 = 1/c^2$ is deduced. The thermal velocity of the cold protons and helium are 0.018 and 0.009 respectively. The thermal velocity of the hot protons is 1.8 and 2.55 for the parallel and perpendicular direction respectively.

The grid spacing is $\Delta x = 1$ and the time step Δt is set equal to 0.05. The number of grid points is 64 and the system length is $L_x = 64$. The number of superparticles in the system is 4096 for each of the cold species. As for hot protons, which are a free energy source in the system, a relatively large number of superparticles (32768) is necessary in order to make the initial thermal fluctuation noise low.

III Simulation Results

The GEOS data suggest that the anisotropic proton distribution excites ion cyclotron waves, which are responsible for heating the thermal helium ions. In order to test this hypothesis, we have run the simulation code up to $\Omega_H t = 1200$. We will first consider the initial phase of the process.

In Figure 1, we see the time history of the magnetic and electric field energy densities for an early stage of the simulation run. Both the magnetic field and electric field energy densities increase throughout the time presented in this plot. The perpendicular component of the electric field is much larger than the parallel one, indicating that charge neutrality is conserved by the predictor-corrector code and that the wave is purely electromagnetic. It should be noted that the magnetic field amplitude attains a very large amplitude: $B_{wave}/B_0 = 0.055$ at $\Omega_H t = 200$. Figure 2a, shows the hot proton energy density in a direction perpendicular and parallel to the ambient magnetic field. Initially at time $\Omega_H t = 100$, the temperature anisotropy decreases only slightly to $(T_\perp/T_\parallel)_h = 1.9$. Later on, the temperature anisotropy decreases more dramatically, as the waves attain large amplitudes, so that at $\Omega_H t = 200$, $(T_\perp/T_\parallel)_h = 1.6$, thus, the hot anisotropic proton distribution is responsible for the growth of these waves. The lower panels (2b) and (2c) show the energy density of thermal helium and protons respectively. Both thermal ion species are accelerated mainly in a direction perpendicular to the ambient magnetic field, with helium ions being preferentially accelerated. We will discuss this acceleration phenomenon later and we will show that it is in fact a two-step process.

To identify the wave mode during the early stages of the simulation run, we plot the dispersion characteristics of the wave. This is done by Fourier transforming individual k modes in time. Figure 3 is a plot of frequency ω versus wavenumber k for the B_y component of the magnetic field during the time interval $\Omega_H t = 1-204$. The amplitude of the wave is denoted

by the height of the peak. It is well known from linear theory analysis (e.g. Gendrin and Roux, 1980; Gendrin, 1981) that the addition of thermal helium breaks the dispersion relation into two branches, one below the helium gyrofrequency known as the low frequency branch (LF) and one above the helium gyrofrequency referred to as the high frequency branch (HF). In fact the LF branch and HF branch are clearly depicted here. The fastest growing frequency occurs in the LF branch with ω/Ω_H = 0.16, kV_A/Ω_H = 0.29 and B_w/B_o = 0.023. The dashed line is the real part of the dispersion relation calculated from the linear theory for the parameters at $\Omega_H t$ = 100. By comparing the dashed line and the plot of the simulation results, the agreement between the real part of the linear dispersion relation and the simulation results are obvious.

To understand the time evolution of the wave properties during the linear stage we plot the time history of four dominant modes in Figure (4a).

The value of k, the wavenumber is related to the mode number m. In fact $k = (2\pi/L_x)m$ where L_x is the system length. Thus for $m = 1$., kV_A/Ω_H =0.1 whereas for m=2, kV_A/Ω_H =0.2, since L_x = 64, V_A = 1 and Ω_H = 1.0.

In Figure (4b) we plot the linear growth rate versus k for both the LF and HF branch. From the upper panel we see that the mode 4, kV_A/Ω_H =0.4 attains a large amplitude at an early time. The growth rates of these modes are found by calculating the slope of the straight dashed line shown in Figure 4. It is found that both of the growth rates of mode 3 and 4 are γ/Ω_H = 0.02. Linear theory (Figure 4b) predicts the peak growth rate to be γ/Ω_H = 0.022 and to occur at $kV_A/\Omega_H \simeq$ 0.3 in agreement with the simulation.

Having ensured that we can reproduce and understand the linear theory from our simulation study we now examine the non-linear physics of the interaction.

In Figure 5 we plot the time history of the magnetic and electric

energy densities throughout the run. As noted previously, the magnetic field increases until about $\Omega_H t = 250$, reaching a peak value $B_w/B_0 = 0.06$ and then remains at a constant amplitude. The electric field behavior is similar, but the peak amplitude in this case is much smaller. $E_w/(B_0 c) = 1.4 \times 10^{-4}$. In a one dimensional system, the peak amplitude is representative of saturation, since the wave energy cannot be lost by coupling to obliquely propagating waves and therefore remains constant. Throughout the simulation run less than 0.2% of the total energy is lost demonstrating that computing errors are negligible and that the energy of the system is conserved.

The time history of the different particle species (Figure 6) is a most enlightening and interesting plot. Panels (a) and (b) show the behavior of the hot anisotropic ions as a function of time. In panel (a) we see that the hot protons are losing energy in a direction perpendicular to the ambient magnetic field. This results in wave growth which in turn causes an increase in the hot proton parallel energy. This expected tendency towards an isotropic hot proton distribution is best seen in Panel (b) where we plot $(T_\perp/T_\parallel)_h$ as a function of time. It is interesting to note that the temperature anisotropy decreases rapidly until $\Omega_H t = 360$, reaching an anisotropy of $(T_\perp/T_\parallel)_h = 1.3$. At later times, the anisotropy does not change significantly, but reaches a value of 1.2 at the end of the run. Panels (c) and (d) show the large heating suffered by the helium ions. In fact, we see that the thermal helium has been heated about 100 times its initial value. We also note that most of the heating is in the perpendicular direction. Thermal protons are also heated but to a much lesser degree.

The snapshots of phase space plots v_x-x, v_y-x at different times for helium ions (Figure 7) and thermal protons (Figure 8) show complex nonlinear structure. Initially, at time $\Omega_H t = 0$, the helium ions are uniformly distributed in phase space. At later times, $\Omega_H t = 100$, we see a

perturbation in v_y. This perturbation occurs from a simple $E_w \times B_o$ force. and results in a transverse motion of the plasma. Later on. $\Omega_H t = 300$ we see that the v_y is about the same except that the amplitude of the oscillations is larger. and tends towards smaller wavenumbers. At that time. we note oscillations in the parallel velocity v_x. In fact the oscillations appear to be folding on themselves. This is because. as the perturbation in the transverse velocity occurs. the particles experience a force $\delta v_{y.z} \times \delta B_{z.y}$ in the parallel direction. At $\Omega_H t = 400$. the motion is extremely nonlinear. with large striations and large oscillations. The motion is so nonlinear that a mixing of plasma. which was originally in different locations. is occurring. resulting in a hotter distribution. Similar nonlinear motions are present in the hydrogen phase space plots (Figure 8) but they are not as prevalent as for helium ions (Figure 7). The reason for that can be seen from the linearized momentum equation of motion for each species.

$$m_j \frac{\partial v_j}{\partial t} = q_j (E_w + v_j \times B_o) \qquad (8)$$

and Maxwell equation

$$\nabla \times E_w = - \frac{\partial B_w}{\partial t} \qquad (9)$$

Solving for v_j. we get

$$v_j = - \frac{\omega}{k} \frac{B_w}{B_o} \frac{1}{(1 - \omega/\Omega_j)} \qquad (10)$$

where $\Omega_j = (q/m)_j B_o$.

Thus. the species response is proportional to B_w and depends on the mass through the resonant denominator. This is why the effect is less dominant for the case of a hydrogen plasma. As the plasma evolves. $v_j \times B_w$ forces become substantial. resulting in a nonlinear motion along the field

lines. This accounts for the late time behavior when 'spirals' develop in the phase space and to a lesser extent in hydrogen.

This 'weaker' spiraling for thermal protons is caused by the fact that the fastest growing wave is in the LF branch, so that the resonant velocity is far from the thermal velocity of protons. In Figure 9 we show the Fourier analysis of the wave properties, during the nonlinear stage of the simulation $\Omega_H t = 800 -1200$. We have decomposed the wave into the forward and backward traveling components. It is found that both the forward and backward traveling waves have equal amplitudes, and only the LF branch has a considerable amplitude. The maximum growth rate $\gamma/\Omega_H = 0.016$ has shifted to lower wavenumbers. The dominant wavenumbers are best seen in Figure 10. where in the upper panel we plot a three-dimensional plot of the amplitude of the wave magnetic field versus k. as a function of time. Looking at Panel (a) it is easy to see that as time proceeds the wave with the largest amplitude occurs at longer wavelength. This tendency towards longer wavelengths can also be seen in the lower panel where we plot the time history of the amplitudes of the four dominant modes. Initially, mode 3 and 4 seem to be mostly responsible for the large amplitude wave observed; however, at later times the amplitude of mode 2 is larger. From linear theory analysis the shifting of the fastest growing modes to lower wavenumbers could be due to either the heating of the helium ions or to the decrease in temperature anisotropy of hot protons [Gendrin et al., 1984. Figure (7a), Figure (7b)].

However, as can be seen on the referenced figures, the reduction in the bandwidth of the unstable waves is more drastic in the first case than in the second. Besides, since the most amplified wave belong to the LF branch of the dispersion curve, a decrease of the hot proton anisotropy has almost no consequence on the frequency of the maximum growth as long as the anisotropy remains above the critical value [Kennel and Petschek, 1966] which corresponds to it. The critical anisotropy is defined by:

$$\omega/\Omega_H = A_C/(A_C + 1) \qquad (11)$$

where $A_C = T_\perp/T_\parallel - 1$.

For $\omega/\Omega_H = 0.1$, $A_C \sim 0.2$. Consequently the frequency of the fastest growing wave is not much affected by a decrease in the hot proton anisotropy as long as $(T_\perp/T_\parallel)_h \geqslant 1.2$. On the other hand, an increase of the hot proton parallel energy, as evidenced by the simulation (see Figure 6), may be at the origin of the decrease of the most amplified wave frequency (see e.g. [Gendrin et al., 1971, Figure 6]).

To test which of these factors is responsible, we ran the simulation by starting with hotter thermal proton and helium distributions, $T_\perp = T_\parallel = 17$ eV, while keeping all the other parameters constant. In this later simulation, the helium ions were only heated by a factor of 2, while the hot proton anisotropy decreased from 2 to 1.25 (still larger than 1.2) and while their parallel energy increased by a factor of 1.4. The shift to lower wavenumber was still observed. These results suggest that neither the heating of the helium ions nor the decrease in temperature anisotropy of the hot protons is responsible for the lowering of the most amplified wavenumber. We therefore conclude that the shift to lower wavenumber is due to the increase of the hot proton parallel energy.

IV Discussion and Conclusion

In this paper using simulation, we have studied the bulk heating of helium ions starting from an initial anisotropic proton distribution. We have shown that the thermal ions are heated to one hundred times their initial temperature, due to the growth of large amplitude ion cyclotron waves. Before discussing the heating mechanism of the helium ions and the saturation of the ion cyclotron waves, let us briefly summarize our findings.

Wave properties:

1) Large amplitude ion cyclotron waves with peak amplitude $B_w/B_o = 0.06$ are observed to grow, due to the temperature anisotropy of the hot proton distribution.

2) Analysis of dispersion properties, frequency and wavenumbers, shows that the presence of helium breaks the dispersion relation into two branches, one below the helium gyrofrequency (LF branch) and one above the helium gyrofrequency (HF branch). This is in agreement with previous work on the linear theory dispersion (see, for example, Gendrin and Roux [1980]).

3) At the early stage of the simulation, agreement with linear theory is very good. The fastest growing mode occurs on the LF branch with $\omega/\Omega_H = 0.16$, $kV_A/\Omega_H = 0.3$ and $\gamma/\Omega_H = 0.02$, where as linear theory predicts $\omega/\Omega_H = 0.17$, $kV_A/\Omega_H = 0.31$ and $\gamma/\Omega_H = 0.022$.

4) The magnetic field reaches a peak amplitude at time $\Omega_H t = 150$ and oscillates about a constant value thereafter.

5) At later times, the fastest growing mode shifts towards longer wavelengths but remains in the low frequency branch. Spectral analysis for the time period between $\Omega_H t = 800$ and $\Omega_H t = 1200$ shows that the fastest growing mode is at $\omega/\Omega_H = 1.1$ and $kV_A/\Omega_H = 0.2$. As discussed in section III, we believe this shift to a lower k mode is due to an increase of the hot proton parallel energy.

63

Particle properties:

1) The hot anisotropic distribution tends towards isotropy with time. The temperature anisotropy changes from $T_\perp/T_\parallel = 2$ at $\Omega_H t = 0$ to $T_\perp/T_\parallel = 1.3$ at $\Omega_H t = 360$ and then changes only slightly until the end of the run.

2) The thermal protons are only slightly heated during the run. As noted previously, this is because of the fact that the fastest growing wave is in LF branch, causing the resonance velocity to be far from the thermal velocity of the protons.

3) The cold helium ions are greatly heated, mostly in the perpendicular direction. The perpendicular helium temperature is about 150 eV whereas the parallel temperature is about 70 eV. Most of the perpendicular heating occurs before $\Omega_H t = 360$, whereas the parallel heating continues until $\Omega_H t \simeq 600$.

4) Phase space plots for helium ions, and to a lesser extent hydrogen ions, show an interesting structure. At the early stages we see oscillation in the v_y component, which is simply due to an $E_w \times B_0$ force. As time evolves these oscillations grow causing a significant $\delta v_{y,z} \times \delta B_{z,y}$ force in the $v_\parallel$ direction. This results in spiraling and complex nonlinear motion in the $v_\parallel$-x phase space plots. At later times, we observe thermalization of the helium ion distributions.

With these observations in mind we can now discuss the saturation mechanism and the heating of helium ions. First let us discuss saturation of the wave. If we calculate the linear growth rate using plasma parameters at the time of peak amplitude $\Omega_H t = 250$, we find a positive growth rate. In fact, for hot proton temperature $T_\parallel = 20$ keV, $T_\perp/T_\parallel = 1.5$, cold proton temperature $T_\parallel = 6$ eV, $T_\perp/T_\parallel = 2$, and helium temperature $T_\parallel = 30$ eV, $T_\perp/T_\parallel = 3.3$, we find from linear theory calculation $\gamma/\Omega_H = 0.012$.

The growth due to positive anisotropy must be balanced by a damping

64

mechanism. One obvious candidate for this damping is trapping of heliums by electromagnetic waves. Evidence for particle trapping can be seen in the phase space plot v_x-x in Figure 7. In fact we calculate the trapping frequency for the mode 4 wave

$$\omega_{trap} = (kB_w \frac{q}{m} v_\perp)^{1/2} \qquad (12)$$

substituting for k = 0.4, B_w =0.02, q/m = 0.25 and $v_\perp$ = 0.1, at $\Omega_H t$ = 250, we find ω_{trap} =014. Equating $\omega_{trap} \sim \tau_{damp}$, we find that the damping rate is of the same order of magnitude as the growth rate.

Now we turn to the problem of heating the helium ions. First, before discussing this, we would like to find out whether the heating is bulk heating or simply high energy tail formation. To do that we plot in Figure 11 the distribution functions of helium ions in the parallel direction as well as the distribution of helium ions in v_y, one of the perpendicular components, at various times. The dashed lines are the initial distribution function. Looking at the left column, we note that at time $\Omega_H t$ = 20 there is some heating. However, at later times the distribution is much hotter. Moreover, this plot shows that indeed we do have bulk heating, as opposed to high energy tail formation.

Now looking at the time history plot (Figure 6) we see that the heating of helium seems to start from the very beginning. Yet the thermal velocity of helium is such that it is difficult to understand how heating takes place. To understand the exchange of energy between the helium ions and the wave, we calculate $E \cdot v_\perp$. In the regions where $E \cdot v$ is positive, the helium ions are gaining energy from the waves and vice versa. We note that in general during the initial phase, $E \cdot v$ is positive whereas it is generally negative later. What we believe is happening is that during the initial phase, while particles are accelerated by the wave there is no heating since the helium ions are far from the resonance velocity. We therefore advance the following scenario. Initially, the helium ions are

65

set into oscillation (no temperature increase) in both the perpendicular and parallel directions by fields of the growing wave. When $v_\perp$ reaches a value near the resonance velocity such that heating can occur, we should see a sudden increase in the perpendicular temperature. We define a resonance region in the velocity phase space as

$$V_R - V_{trap} < v_\parallel < V_R + V_{trap} . \tag{13}$$

where V_R is the resonance velocity given by $(\omega - \Omega_{He})/k$, and V_{trap} is the trapping velocity given by $2\omega_{trap}/k$. In the resonance region nonlinear trapping of heliums is possible, leading to the heating. The above scenario is consistent with the lower panel of Figure 6, where the cold helium temperature increases from the beginning of the run. The temperature plotted there is actually the space-averaged temperature, and the oscillatory effects of the waves have been averaged over many wavelengths giving an apparent velocity spread and temperature in a region of space a quarter of the wavelength of mode 4 in each direction. In Figure 12 we show such a local perpendicular temperature diagnostic and also the number of helium ions whose velocity lies within the resonance region for the mode 4 wave ($V_R = -0.16$, $V_{trap} \simeq 0.07$). At first there are no particles and there is no increase in temperature. Later the number of particles has increased and we have a sudden surge in temperature. These diagnostics clearly indicate that the energy gained by the heliums during the linear phase is transfered to thermal motion due to the nonlinear trapping.

The results which have been presented show the efficiency of the simulation code to interpret complex wave particle interactions in a multicomponent plasma. Some interesting results have been obtained which concern the heating of heavy ions in the equatorial magnetosphere by ICW's. However, more experimental runs have to be performed and some improvements are still needed to answer specific questions related either

with the physics of the phenomenon or to the efficiency of the simulation code.

As far as physics is concerned, there remain some discrepancies between the simulation results and experimental data. A drastic lowering in the frequency of the most amplified wave found in the simulation is generally not observed in experimental data. The delay which is observed between the establishment of a rather large wave field and the heating of He^+ ion is much shorter in the simulation run than it seems to be in the case of experimental data [Young et al., 1981; Roux et al., 1982]. The bunching of He^+ ions, which is a striking feature of ATS-6 observations [Mauk et al., 1981] is not as clearly reproduced in the results of the simulation.

Some of these discrepancies can be explained by the fact that the numerical runs reproduce a stationary case, and not a progressive one, because a periodic boundary condition is assumed in the present simulation. Waves cannot escape, and new hot particles are not injected, thus preventing the simulation system to represent an equilibrium where input and output energy flows are balanced. The size of the system should be increased ($L_x \geqslant 128$) in order to be able to follow in more detail the evolution of the most amplified wavenumber. Finally, a parametric study (number of particles per cell, more efficient predictor-corrector schemes, ...) should be undertaken in order to optimize the cost/efficiency of the operational code which has been so successfully used throughout this study.

Figure Captions

Figure 1. Time history of the magnetic and electric energy densities during the early stages of the simulation. We note that both the magnetic field and electric fields are still growing at time $\Omega_H t = 200$. The dashed line on the lower panel reflects the variation of E_x, the smallness of which demonstrates the efficiency of the code and the electromagnetic nature of the wave.

Figure 2. The time history of the energy densities of the hot protons (panel a), helium ions (panel b) and thermal hydrogen (panel c). Note that the temperature anisotropy hardly changes until time $\Omega_H t = 100$ and then the decrease is more rapid. Both thermal species show an increase in energy density, preferentially in the perpendicular direction.

Figure 3. We plot the dispersion relation of the B_y component during the early phase of the simulation $\Omega_H t = 204$. We also plot the theoretical linear dispersion relation by dashed lines using the plasma parameters at $\Omega_H t = 100$. We observe that both the simulation results and the linear theory show the dispersion relation separated into two branches; the high frequency branch (HF) above the helium cyclotron frequency and the low frequency branch (LF) below the helium cyclotron frequency. The fastest growing frequency occurs in the LF branch at $\omega/\Omega_H = 0.16$ and $kV_A/\Omega_H = 0.29$.

Figure 4. In the upper panel we plot time evolution of the four dominant modes during the linear phase of the simulation. The lower panel shows the theoretical linear growth rate as a function of wavenumber. From the upper panel we find that the growth rates for mode 3 and 4, corresponding to $kV_A/\Omega_H = 0.3$ and $kV_A/\Omega_H = 0.4$ respectively, are $\gamma/\Omega_H = 0.02$. The lower panel predicts the peak growth rate to be $\gamma/\Omega_H = 0.022$ at $kV_A/\Omega_H = 0.3$.

Figure 5. Time history of the electric and magnetic energy densities until

the end of the run. The magnetic energy density increases until about $\Omega_H t = 300$, reaching a peak amplitude $B_w/B_O = 0.06$. Saturation occurs about $\Omega_H t = 300$.

Figure 6. A time history of the different particle species, the hot protons panels (a) and (b), the perpendicular temperature of helium and thermal protons panel (c) and the parallel temperature of helium and thermal protons panel (d). We note in panels (a) and (b) that the anisotropy decreases rapidly until about $\Omega_H t = 360$, reaching a value of $T_\perp/T_\parallel = 1.3$. At later times the He^+ ions have been heated about 100 times the initial value in the perpendicular direction. Most of the heating occurs prior to $\Omega_H t = 500$. The H^+ ions are also heated in the parallel but to a lesser degree. Thermal protons are only slightly heated.

Figure 7. Phase space plot for He^+ at different times. The left column is in v_y-x space, while the right column is in v_x-x space.

Figure 8. A phase space plot for thermal hydrogen at different times. The left column is in v_y-x space while the right column is in v_x-x space.

Figure 9. A figure of the dispersion relation of the B_y component during the nonlinear stage of the simulation $\Omega_H t = 800-1200$. The upper panel is for the forward traveling wave, while the lower panel is for the backward traveling wave. At this stage of the simulation only the LF branch has a considerable stimulation. The dashed line represents the linear dispersion relation calculated from the pa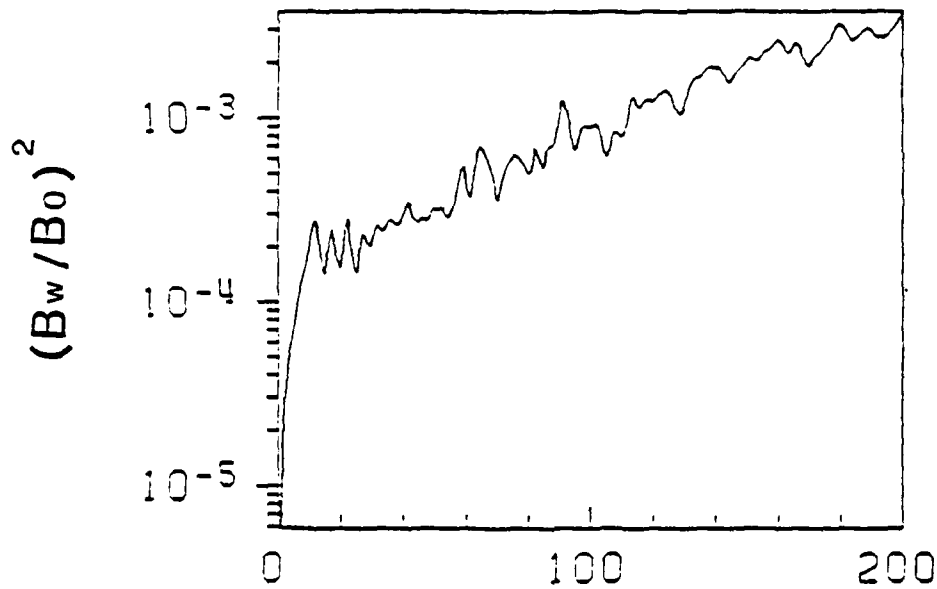rameters at $\Omega_H t = 1000$. Figure 10. Panel (a) shows the time evolution of the k-spectra of the wave magnetic field, while panel (b) shows the amplitude versus time of the dominant modes in the system. Note how the fastest growing modes shift to lower wavenumbers with time.

Figure 11. A plot of the distribution function of thermal helium at three different times. The left column is the parallel distribution function, whereas the right column is the distribution function in one

of the transverse directions. The dashed line is the initial distribution function at time $\Omega_H t = 0$. Note the broadening of the distribution function $f(v_\perp)$ at time $\Omega_H t = 400$. Looking at the lower left panel we see that the helium continues to heat until the end of the run, but at a slower rate.

Figure 12. Here we plot certain diagnostics needed to understand the heating mechanism of thermal helium. At panel (a), we plot $E_\perp \cdot v_\perp$. For $E_\perp \cdot v_\perp \geq 0$, the energy is transferred from the waves to the helium ions and vice versa. We note that most of the energy transfer from the waves to the helium ions occurs prior to time $\Omega_H t = 400$. In panel (b) we plot the effective temperature of the helium, by measuring the temperature in a region of space a quarter of he wavelength of mode 4 in each direction. In panel (c) we plot the number of helium ions whose velocity lies within the resonance region. We note that number of trapped particles and the effective temperature seem to increase simultaneously, at time around $\Omega_H t = 500$.

Magnetic Energy Density
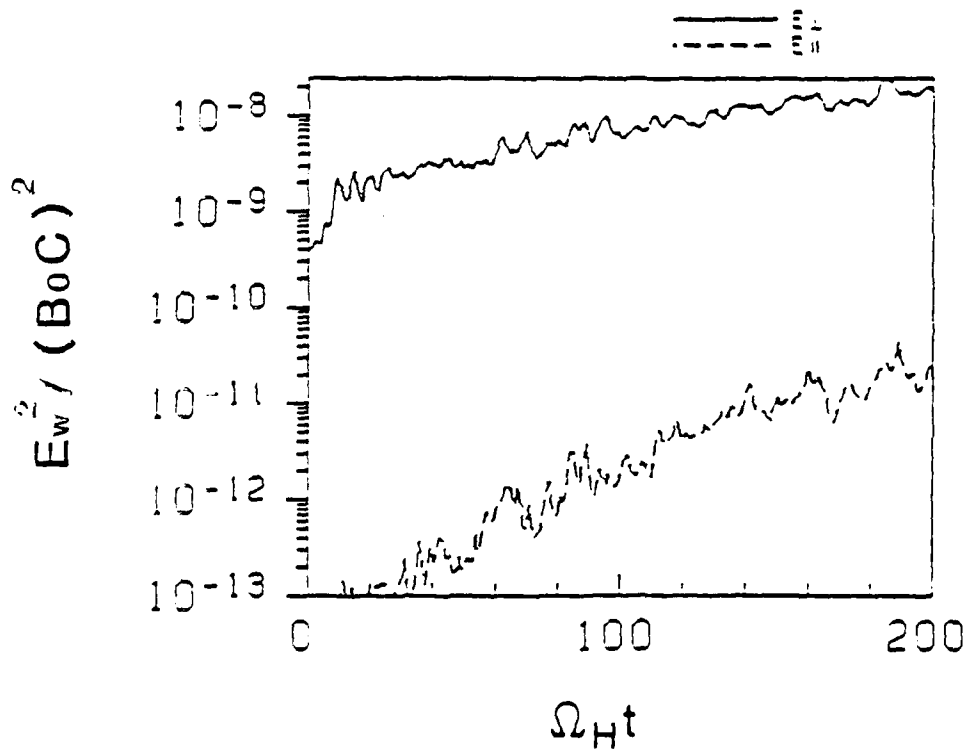

Electric Energy Density

$\Omega_H t$

Figure 1. Time history of the magnetic and electric energy densities during the early stages of the simulation. We note that both the magnetic field and electric fields are still growing at time $\Omega_H t = 200$. The dashed line on the lower panel reflects the variation of E_x, the smallness of which demonstrates the efficiency of the code and the electromagnetic nature of the wave.
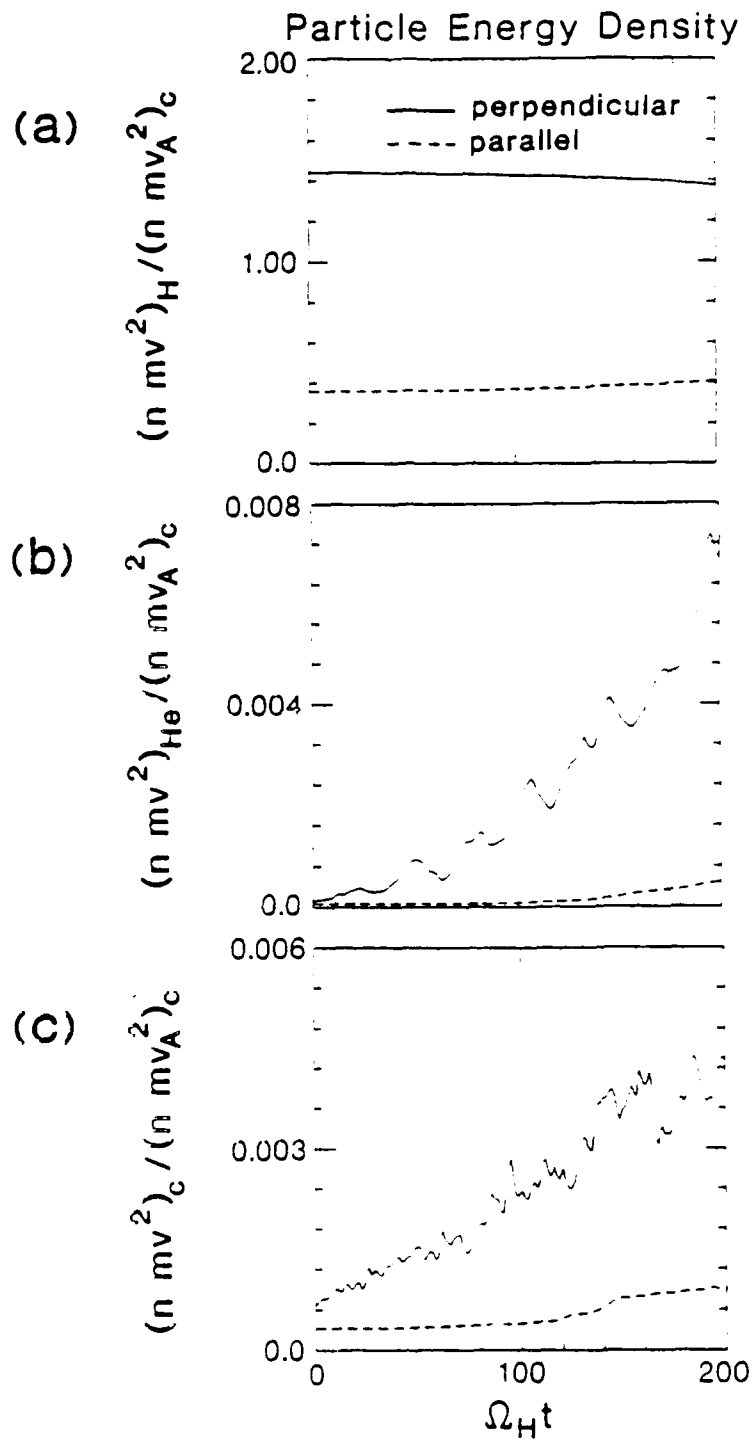
Figure 2. The time history of the energy densities of the hot protons (panel a), helium ions (panel b) and thermal hydrogen (panel c). Note that the temperature anisotropy hardly changes until time $\Omega_H t = 100$ and then the decrease is more rapid. Both thermal species show an increase in energy density, preferentially in the perpendicular direction.
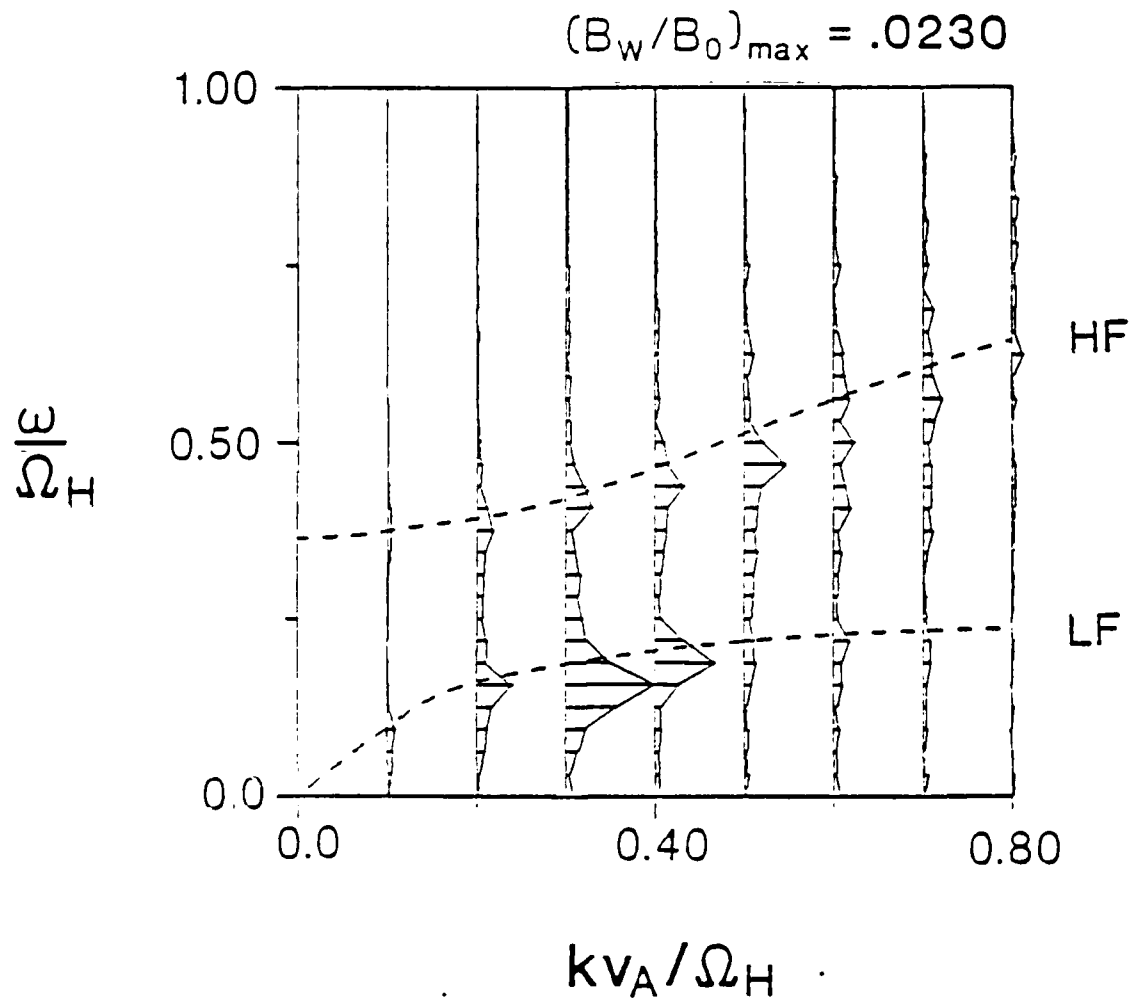
Dispersion Relation

$$(B_W/B_0)_{max} = .0230$$

Figure 3. We plot the dispersion relation of the B_y component during the early phase of the simulation $\Omega_H t = 204$. We also plot the theoretical linear dispersion relation by dashed lines using the plasma parameters at $\Omega_H t = 100$. We observe that both the simulation results and the linear theory show the dispersion relation separated into two branches; the high frequency branch (HF) above the helium cyclotron frequency and the low frequency branch (LF) below the helium cyclotron frequency. The fastest growing frequency occurs in the LF branch at $\omega/\Omega_H = 0.16$ and $kV_A/\Omega_H = 0.29$.

(a) Time History of the Wave Magnetic Field
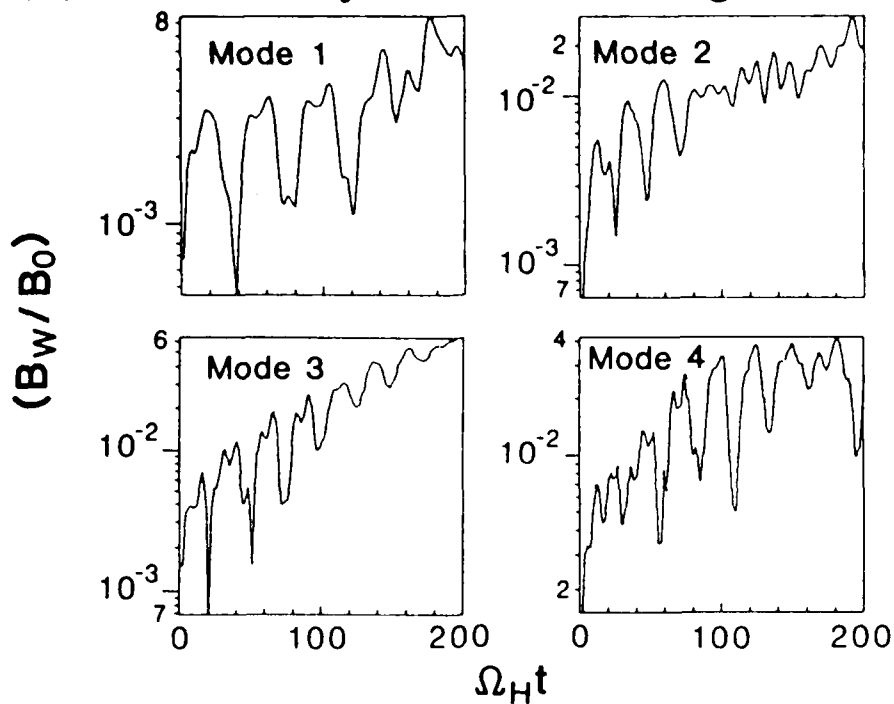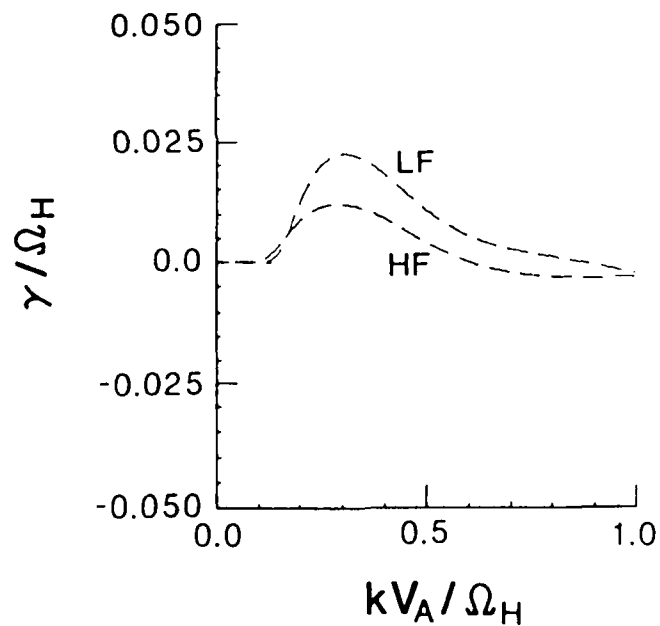

(b) Linear Growth Rates

Figure 4. (a) Time evolution of the four dominant modes during the linear phase of the simulation. (b) Theoretical linear growth rate as a function of wave number. From Figure 4a we find that the growth rates for modes 3 and 4, corresponding to $kV_A/\Omega_H = 0.3$ and $kV_A/\Omega_H = 0.4$, respectively, are both equal to $\gamma/\Omega_H = 0.02$. Figure 4b predicts the peak growth rate to be $\gamma/\Omega_H = 0.022$ at $kV_A/\Omega_H = 0.3$.

Magnetic Energy Density

$$(B_w/B_0)^2$$

10^3

10^4

Electric Energy Density

$$E_w^2 / (B_0C)^2$$

10^{-8}

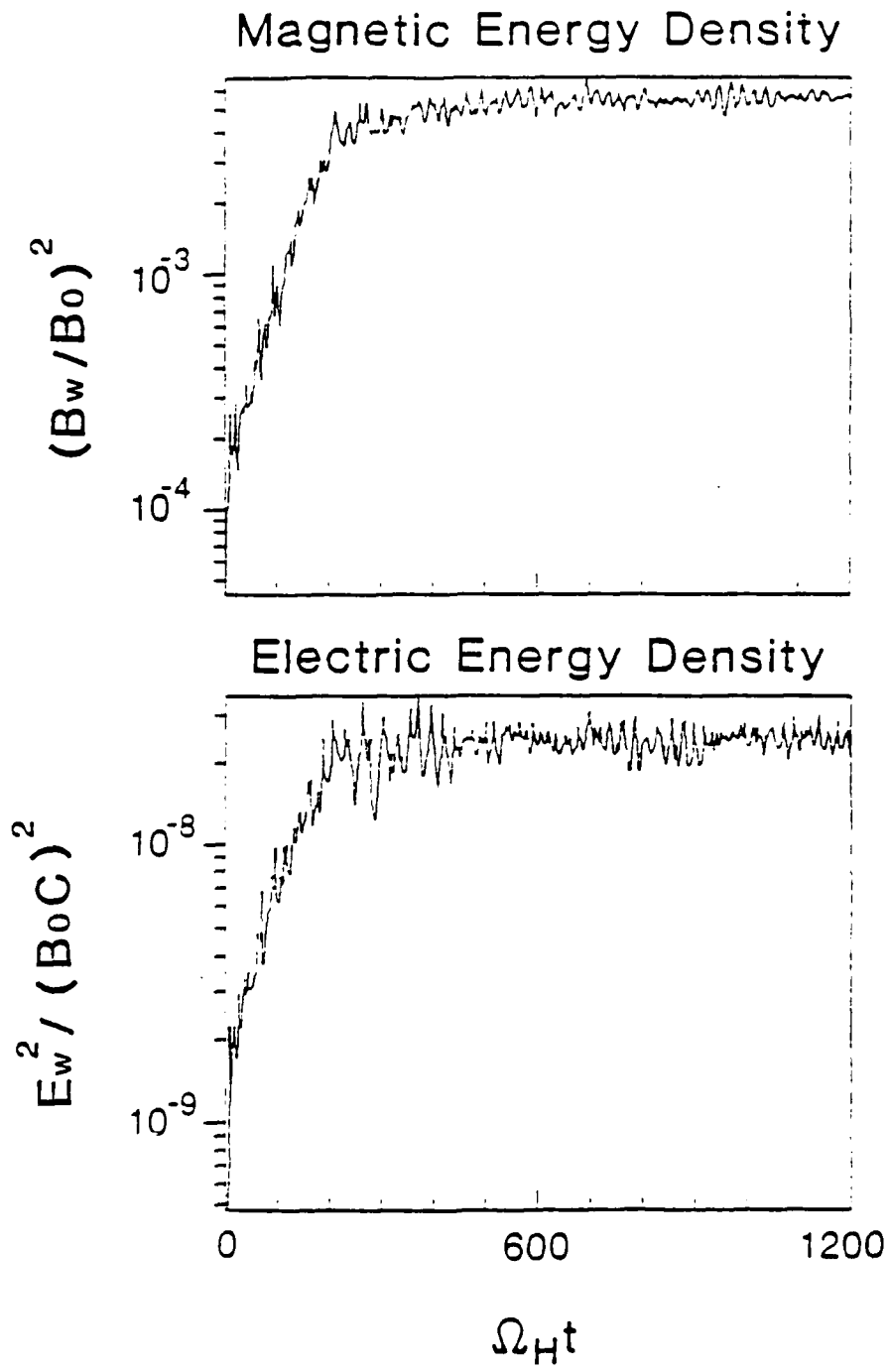10^{-9}

0   600   1200

$$\Omega_H t$$

Figure 5. Time history of the electric and magnetic energy densities until the end of the run. The magnetic energy density increases until about $\Omega_H t = 300$, reaching a peak amplitude $B_w/B_0 = 0.06$. Saturation occurs about $\Omega_H t = 300$.
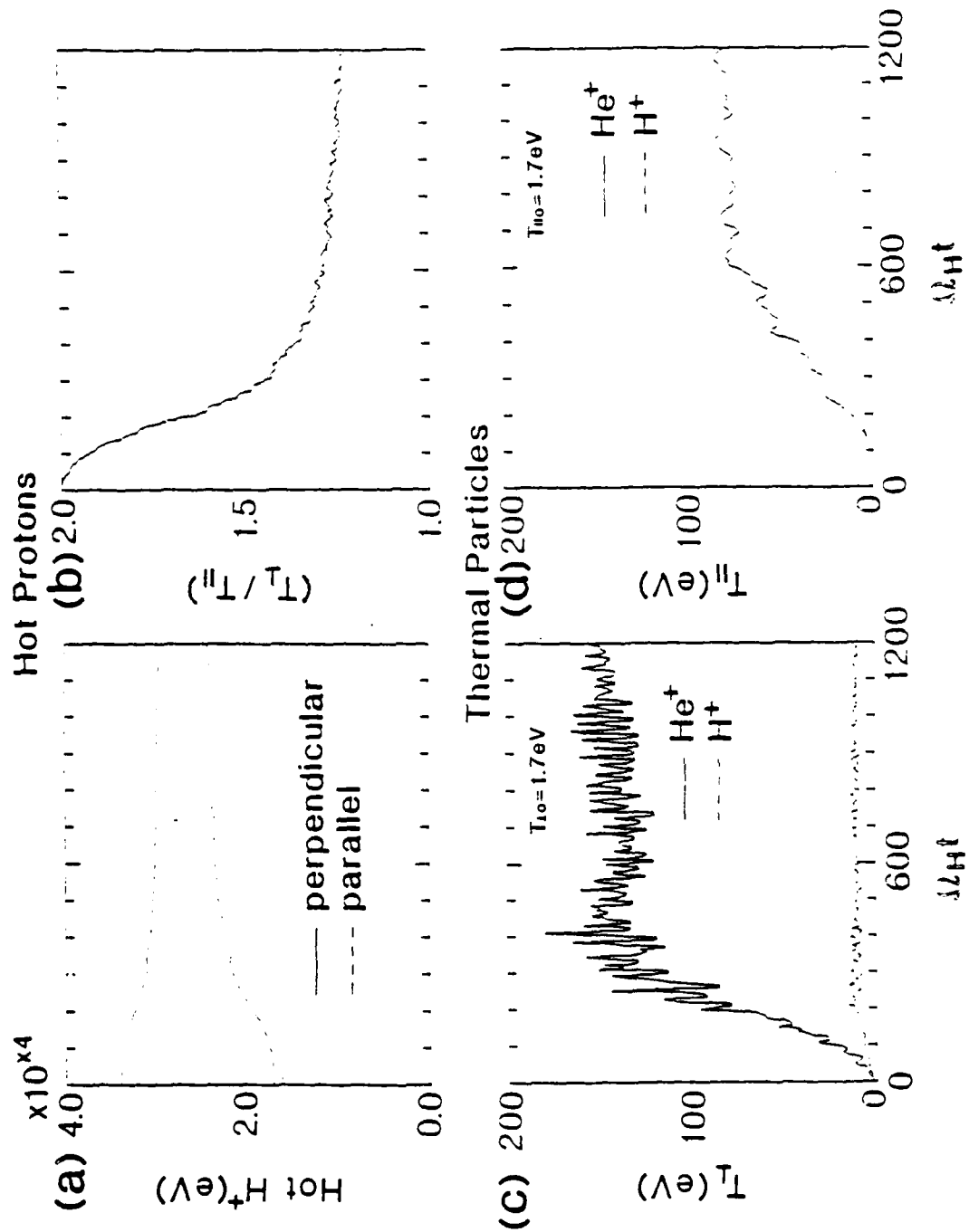
TIME HISTORY OF PARTICLE TEMPERATURES

Figure 6. A time history of the different particle species, the hot protons panels (a) and (b), the perpendicular temperature of helium and thermal protons panel (c) and the parallel temperature of helium and thermal protons panel (d). We note in panels (a) and (b) that the anisotropy decreases rapidly until about $\Omega_H t = 360$, reaching a value of $T_\perp/T_\parallel = 1.3$. At later times the He$^+$ ions have been heated about 100 times the initial value in the perpendicular direction. Most of the heating occurs prior to $\Omega_H t = 500$. The H$^+$ ions are also heated in the parallel but to a lesser degree. Thermal protons are only slightly heated.
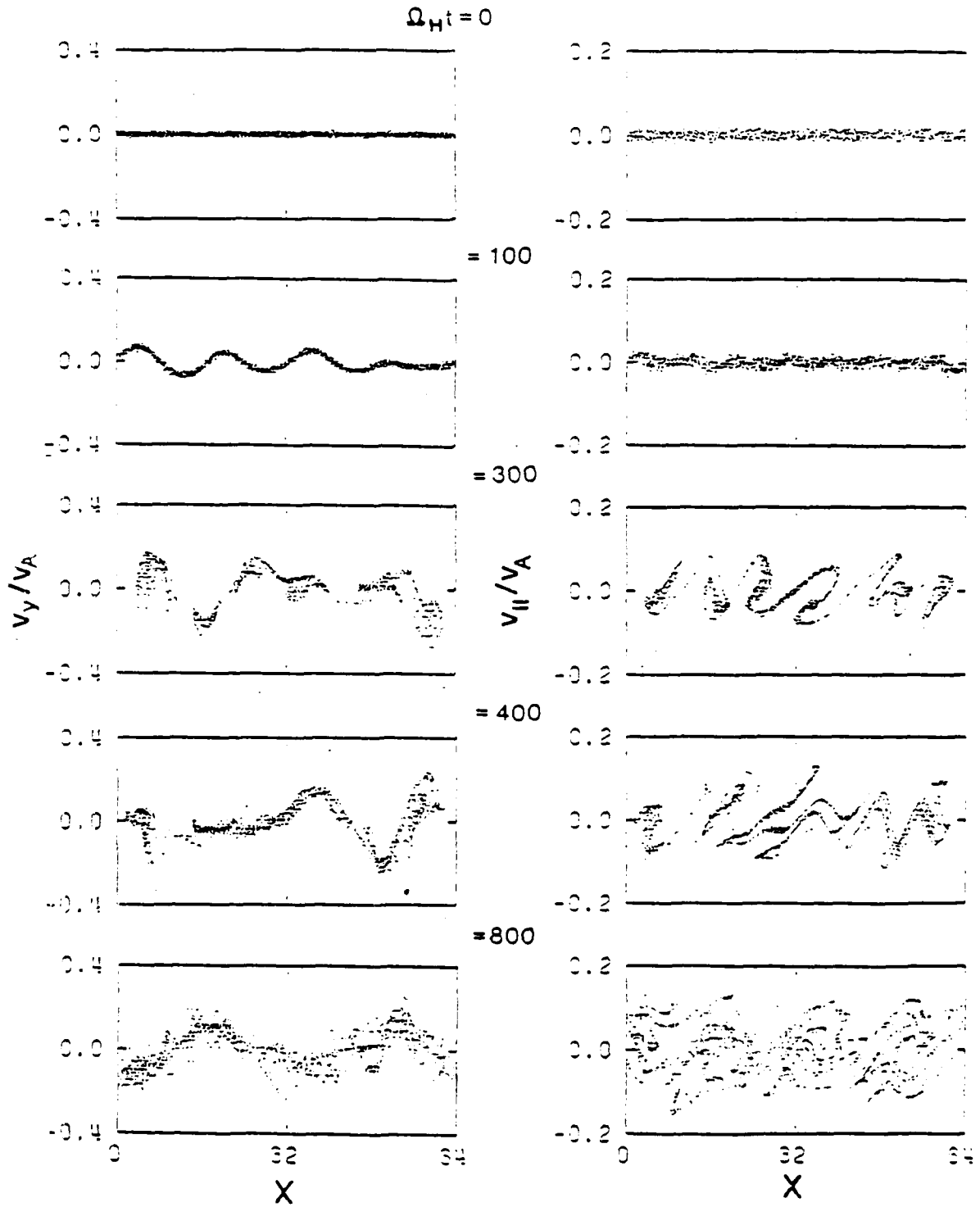
77

Phase Space for He$^+$

Figure 7. Phase space plot for He$^+$ at different times. The left column is in v_y-x space, while the right column is in v_x-x space.
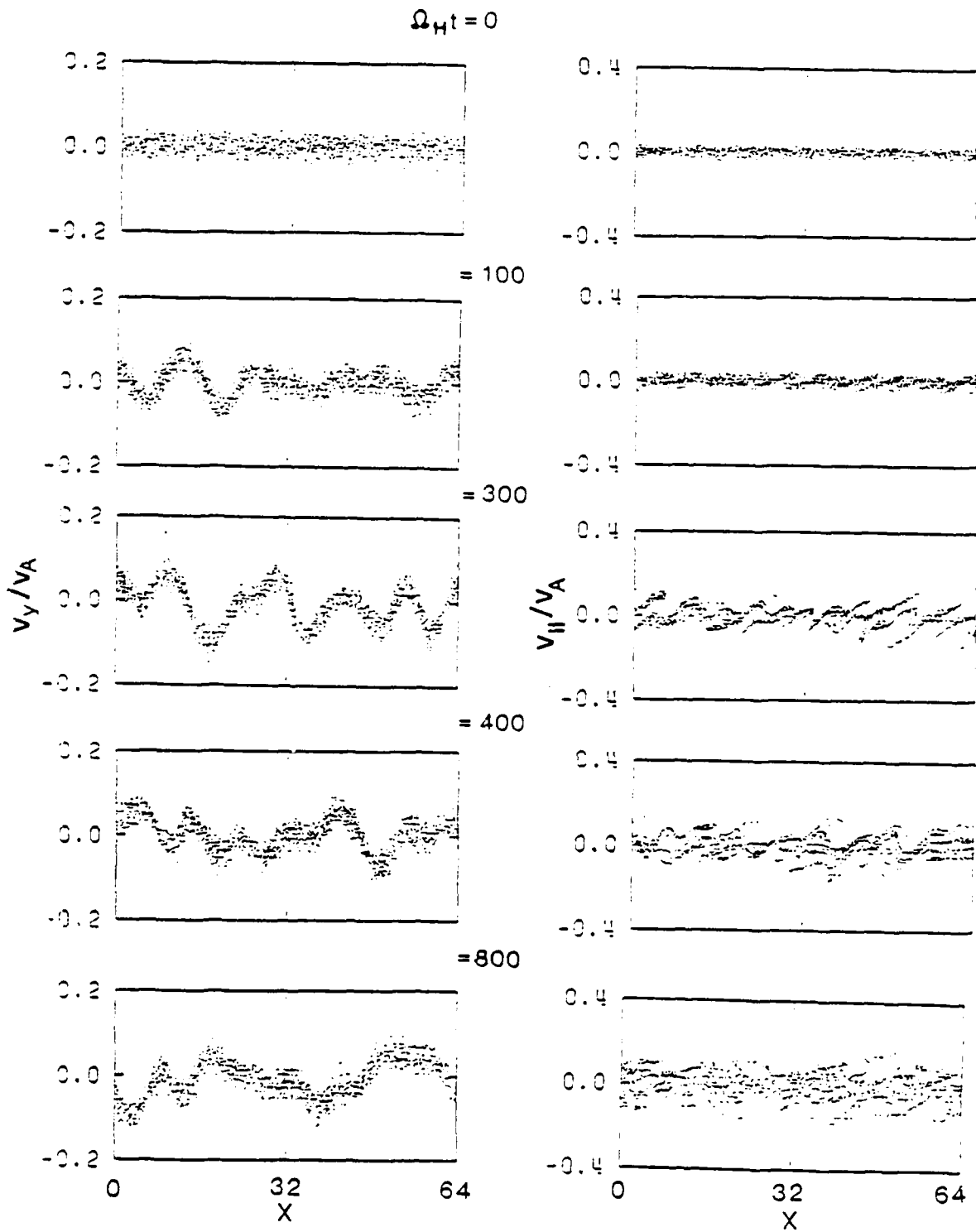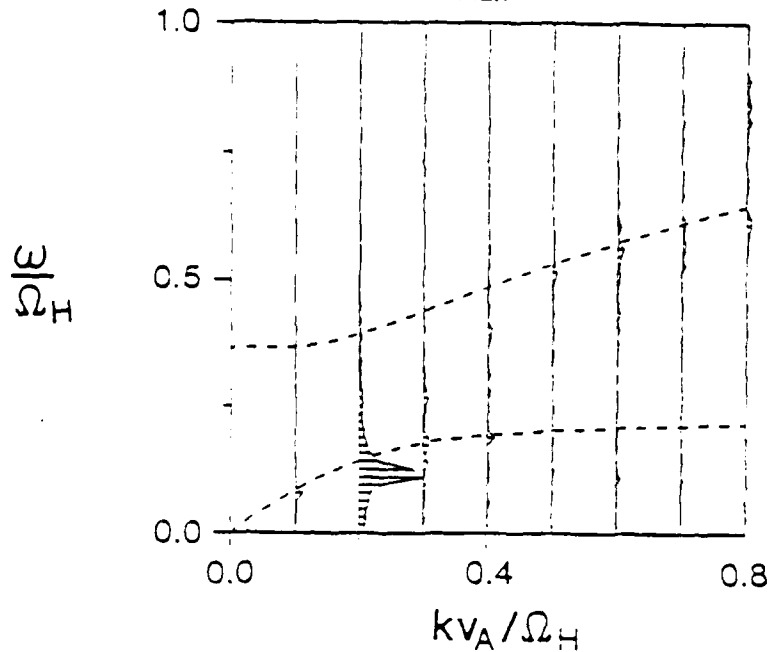
Phase Space for Thermal H⁺

Figure 8. A phase space plot for thermal hydrogen at different times. The left column is in v_y-x space while the right column is in v_x-x space.

Dispersion Relation

Forward Traveling Wave
$(B_w/B_o)_{max} = .0353$

Backward Traveling Wave
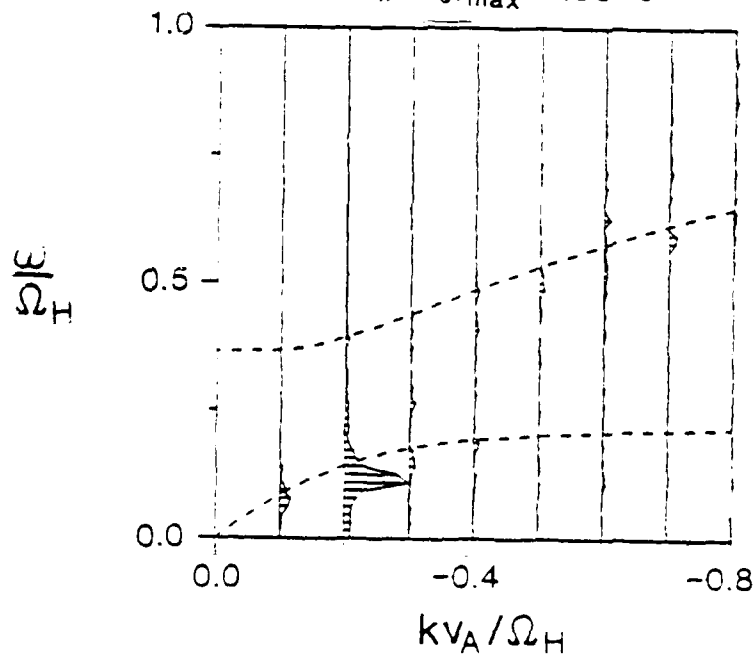### $(B_w/B_o)_{max} = .0346$

Figure 9. A figure of the dispersion relation of the B_y component during the nonlinear stage of the simulation $\Omega_H t = 800-1200$. The upper panel is for the forward traveling wave, while the lower panel is for the backward traveling wave. At this stage of the simulation only the LF branch has a considerable stimulation. The dashed line represents the linear dispersion relation calculated from the parameters at $\Omega_H t = 1000$.
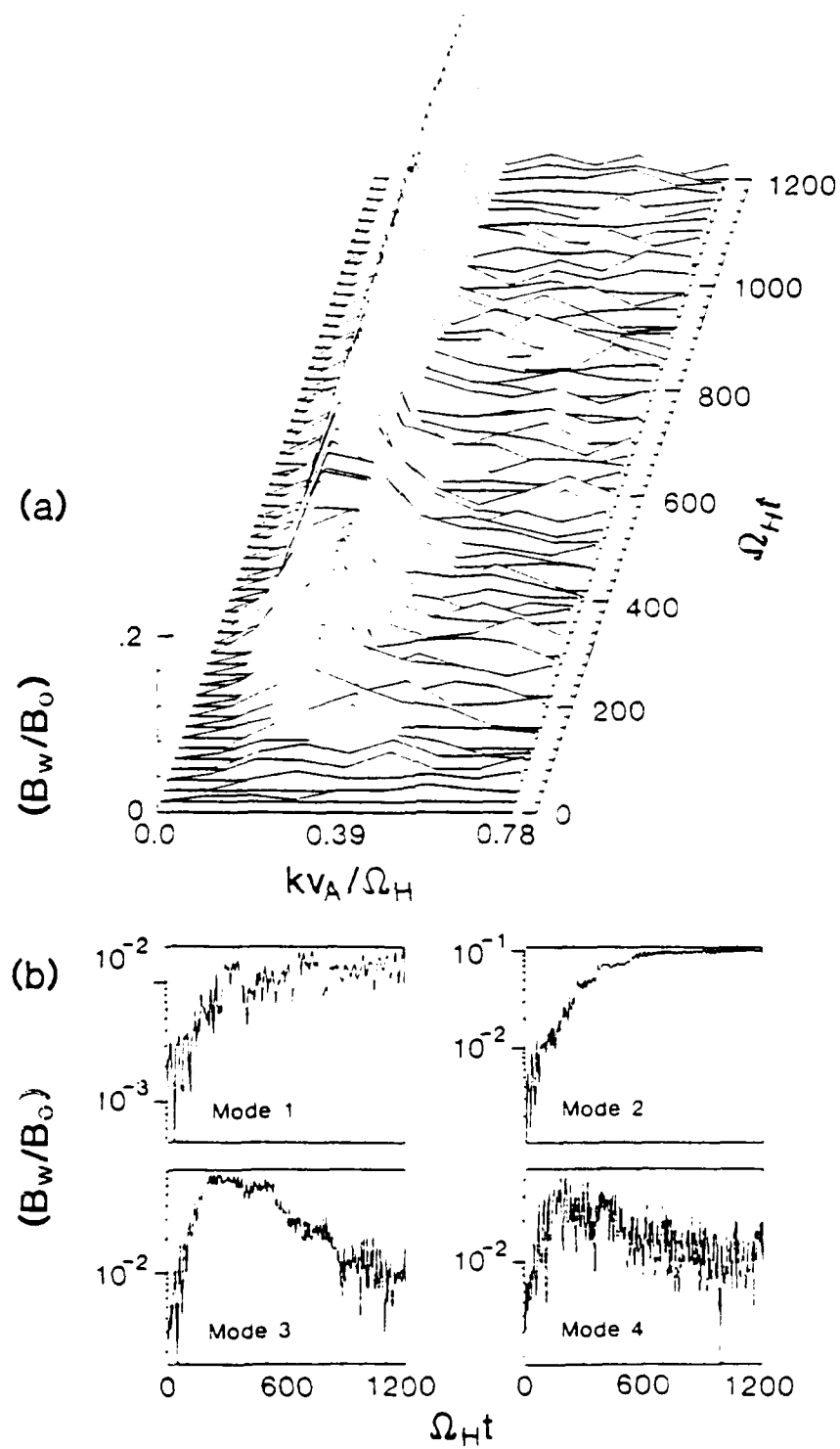
Time History of the Wave Magnetic Field

Figure 10. Panel (a) shows the time evolution of the k-spectra of the wave magnetic field, while panel (b) shows the amplitude versus time of the dominant modes in the system. Note how the fastest growing modes shift to lower wavenumbers with time.

Distribution Functions for He$^+$

Figure 11. A plot of the distribution function of thermal helium at three different times. The left column is the parallel distribution function, whereas the right column is the distribution function in one of the transverse directions. The dashed line is the initial distribution function at time $\Omega_H t$ = 0. Note the broadening of the distribution function $f(v_{\perp})$ at time $\Omega_H t$ = 400. Looking at the lower left panel we see that the helium continues to heat until the end of the run, but at a slower rate.

Figure 12. Here we plot certain diagnostics needed to understand the heating mechanism of thermal helium. At panel (a), we plot $E_\perp \cdot v_\perp$. For $E_\perp \cdot v_\perp > 0$, the energy is transferred from the waves to the helium ions and vice versa. We note that most of the energy transfer from the waves to the helium ions occurs prior to time $\Omega_H t = 400$. In panel (b) we plot the effective temperature of the helium, by measuring the temperature in a region of space a quarter of the wavelength of mode 4 in each direction. In panel (c) we plot the number of helium ions whose velocity lies within the resonance region. We note that number of trapped particles and the effective temperature seem to increase simultaneously, at time around $\Omega_H t = 500$.

83

PPG-793   "A New Electromagnetic Mode in a Non-Maxwellian High-Beta Plasma," J. M. Urrutia & R. L. Stenzel, June (1984).

PPG-794   "Global Inelastic Structural Analysis and Life-Time Estimation for Tubular Fusion Reactor Blankets," James P. Blanchard and Nasr Ghoniem, submitted to Nuc. Engr. & Design, June, 1984.

PPG-795   "Tokamak Plasma Wave Studies Via Multi-Channel Far Infared Laser Scattering," Ilyeon Park, June, 1984.

PPG-796   "A 3-D MHD Simulation of the Interaction of the Solar Wind With the Earth's Magnetosphere: The Generation of Field Aligned Currents," T. Ogino, June, 1984.

PPG-797   "Driven Magnetic Reconnection in Three Dimensions: Energy Conversion and Field Aligned Current Generation," T. Sato, R. J. Walker, M. Ashour-Abdalla, June, 1984.

PPG-798   "Doppler Shift Dominated Cyclotron Masers," A. T. Lin, submitted to International Journal of Electronics. June, 1984.

PPG-799   "Self Consistent Plasma Heating and Acceleration by Strong Magnetosonic Waves for $\theta = 90^\circ$," B. Lembege and J.M. Dawson, submitted to The Physics of Fluids, June 1984

PPG-800   "Electron-Cyclotron Maser Radiation from a Relativistic Loss-Cone Distribution," P. L. Pritchett, submitted to The Physics of Fluids, July, 1984.

PPG-801   "A High-Harmonic Gyro-Kylstron Amplifier: Theory and Experiment," D. S. Furuno, D. B. McDermott & A. C. Luhmann, Jr. & P. Vitello, July, 1984.

PPG-802   "A Plasma Booster for Linear Accelerators," Pisín Chen, R. W. Huff & J. M. Dawson, August (1984).

PPG-803   "Nonlinear Interactions of CO_2 Laser Radiation With Plasmas," F. F. Chen & C. Joshi, Technical Report, July, 1984.

PPG-804   "Stabilization of Ballooning Modes in an Axisymmetric Mirror by a Hot Electron Ring," H. Sanuki, G. J. Morales & B. D. Fried, July (1984).

PPG-805   "A MHD Simulation of the Bidependent Magnetospheric Convections and Field Aligned Currents During North-ward IMS," T. Ogino, R. J. Walker, M. Ashour-Abdalla & J. M. Dawson, July (1984).

PPG-806   "Investigations of Titatium Gettering with Applications to Macrotor and Microtor," J. R. Elliott, L. L. Keller, R.J. Taylor & R.S. William, July (1984).

PPG-807   "Wave Dispersion and Ray Propagation in a Weakly Relativistic Electron Plasma: Implications for the Generation of Auroral Kilometric Radiation," R.J. Strangeway, submitted to J. Geophysical Research, July (1984).

PPG-808 "Experiments on Langmuir Collapse", A. Y. Wong, P.Y. Cheung, Int'l. Conf. on Plasma Physics, July (1984).

PPG-809 "Multichannel Far-Infrared Interferometer/Polarimeter", P.E. Young.

PPG-810 "The k = 0 Mode Contribution in Periodic & Bounded Particle Simulation Codes", B. Lembege and J.M. Dawson.

PPG-811 "Observation of the Externally Excited Fast Magnetosonic wave via Collective Thomson Scattering", H. Park, W.A. Peebles, MC. Luhmann, Jr., R. Kirkwood, R.J. Taylor.

PPG-812 "Multichannel Scattering Studies of the Spectra and Spatial Distribution of Tokamak Microturbulence", W.L. Brower, W.A. Peebles, N.C. Luhmann, Jr., R.L. Savage, Jr., submitted to Phys. Rev. Lett. in July 1984.

PPG-813 "Thermalization of netrual-beam-injected ions by lower hybrid waves in Jupiter's magnetosphere," D. D. Barbosa, August (1984).

PPG-814 "Nonlinear Evolution of Slow Waves in the Solar Wind," T. Hada & C. F. Kennel, August, 1984.

PPG-815 "Technical Assessment of the Critical Issues and Problem Areas in High Heat Flux Materials and Component Development, Volume II," M. A. Abdou, et. al., June, 1984.

PPG-816 "Volume III: Strategies for International Collaborations in the Areas of Plasma Materials Interactions and High Heat Flux Materials and Component Development," W. B. Gauster, et. al, January, 1984.

PPG-817 "Raman Backscatter Below the Absolute Threshold," F. F. Chen, August, 1984.

PPG-818 "Boston Abstracts for the 1984 A.P.S. Meeting," August, 1984, S.T. Ratliff.

PPG-819 "Beat Wave and Surfatron Accelerator of Particles", August, 1984, J.M. Dawson.

PPG-820 "Prospects of the Surfatron Laser Plasma Accelerator", T. Katsouleas, C. Joshi, W. Mori, J.M. Dawson, June, 1984.

PPG-821 "FINESSE: A Study of the Issues, Experiments & Facilities for Fusion Nuclear Technology Research and Development, Interim Report," M. Abdou, et al., September, 1984.

PPG-822 "A Quarter Century of Collisionless Shock Research," C. F. Kennel, J. P. Edmiston, T. Hada, September (1984).

PPG-823 "Stability of Ballooning Modes in an Axisymmetric Mirror by a Hot Electron Ring and a RF Electric Field," H. Sanuki, G. J. Morales & B. D. Fried, October (1984).

PPG-824 "Resonant Instability Near the 2-Ion Cross-over Frequency in the Io Plasma Torus," R. Thorn & J.J. Moses, submitted to JGR, October, 1984.

PPG-825 "Generation of Lower Hybrid Noise by Superthermal Cross-Field Ion Currents," D. D. Barbosa, October (1984).

PPG-826 "Quasi-Thermodynamic Prediction of Hydrogen Re-emission from Titanium Films," Y. Hirooka, R. W. Conn, D. M. Geobel, October (1984).

References

Ashour-Abdalla, M., H. Okuda and C. Z. Cheng, acceleration of heavy ions on auroral field lines, Geophys. Res. Lett., 8, 795, 1981.

Ashour-Abdalla, M., H. Okuda, Turbulent heating of heavy ions on auroral field lines. J. Geophys. Res., 89, 2235, 1984.

Balsiger, H., P. Eberrd, J. Geiss, and D. T. Young, Magnetic storm injection of 0.9 to 1.6 keV/e solar and terrestrial ions into the high-altitude magnetosphere, J. Geophys. Res., 85, 1645, 1981.

Berchem, J., R. Gendrin, and M. Ashour-Abdalla, Acceleration of heavy is by ULF electromagnetic waves, 3. Analytical study of the nonlinear phases (abstract), EOS, 64, 815, 1983.

Berchem, J., and R. Gendrin, Non resonant interaction of heavy ions with electromagnetic on cyclotron waves, Ann. Geophys., submitted to, 1984.

Byers J. A., B. I. Cohen, W. C. Condit, and J. D. Hanson, Hybrid simulations of quasineutral phenomena in magnetized plasma, J. Comput. Phys., 27, 363, 1978.

Chappell, R. C., Cold plasma distribution above a few thousand kilometers at high latitude, in High Latitude Space Plasma Physics, B Hultqvist and T. Hagfors, el., Plenum Pres, p. 251, 1983.

Decreau, P. M. E., C. Beghin, and M. Parrot, Global characteristics of the cold plasma in the equatorial plasmapause region as deduced from the GEOS-1 mutual impedance probe, J. Geophys. Res., 87, 695, 1982.

Frank, L. A., K. L. Ackerson, and D. M. Yeager, Observations of atomic oxygen (O^+) in the Earth's magnetotail, J. Geophys. Res., 82, 129, 1982.

Fraser, B. J., Pc 1-2 observations of hvy ion effects by synchronous satellite ATS-6, Planet. Space Sci., 30, 1229, 1982.

Geiss, J., H. Balsiger, P. Eberhardt, H. P. Walker, L. Weber and, D. T. Young, Dynamics of magnetospheric ion composition as observed by the

GEOS mass spectrometer. *Space Sci. Rev.*. 2. 537. 1978.

Gendrin. R.. S. Lacourly. A. Roux. J. Solomon. F. Z. Feiguin. M. V. Ghberg. and V. A. Troitskaya. Wave packet propagation in an amplifying medium and its application to the dispersion characteristics and to the generation mechanism of Pc 1 events. *Planet. Space Sci.*. 19. 165. 1971.

Gendrin R.. and A. Roux. Energization of helium ion by proton induced hydromagnetic waves. *J. Geophys. Res.*. 85. 4577. 1980.

Gendrin R.. M. Ashour-Abdalla. Y. Omura. and K. Quest. Linear analysis of ion cyclotron interaction in a multi-component plasma. *J.Geophys. Res.*. in press. 1984.

Ghielmetti. A... R. G. Johnson. R. D. Sharp. and E. G. Shelley. The latitudinal. diurnal and altitudinal distributions of upward flowing energetic ions of ionospheric origin. *Geophys. Res. Lett.*. 5. 59. 1978.

Gomberoff. L.. and S. Cuperman. Combined effect of cold H^+ and He^+ ions on the proton cyclotron electromagnetic instability. *J. Geophys. Res.*. 87. 95. 1982.

Gomberoff. L.. and R. Neira. Convective growth rate of ion cyclotron waves in a H^+-He^+ and H^+-He^+-O^+ plasma. *J. Geophys. Res.*. 88. 2170. 1983.

Hardy D. A.. J. W. Freeman. and H. K. Hills. Double-peaked ion spectra in the lobe plasma: evidence for massive ions?. *J. Geophys. Res.*. 82. 5529. 1977.

Isenberg. P. A.. The ion cyclotron dispersion relation in a proton-alpha solar wind. *J. Geophys. Res.*. 89. 2133. 1984a.

Isenberg. P. A.. Resonant acceleration and heating solar wind ions : anisotropy and dispersion. *J. Geophys. Res.*. 89. 6613. 1984b.

kennel C. F.. and H. E. Petschek. Limit on stably trapped particle fluxes. *J. Geophys. Res.*. 71. 1. 1966.

Lysak. R. L.. M. Hudson. and M. Temerin. Ion heating by strong

electrostatic ion cyclotron turbulence. J. Geophys. Res., 85, 678, 1980.

Mauk, B. H., C. E. McIlwain, and R. L. McPherron. Helium cyclotron resonance within the earth's magnetosphere. Geophys. Res. Lett., 8, 103, 1981.

Mauk, B. H., Electromagnetic wave energization of heavy ion by the electric 'phase bunching' process. Geophys. Res. Lett., 9, 1163, 1982.

Mauk, B. H., Frequency gap formation in electromagnetic cyclotron wave distribution. Geophys. Res. Lett., 10, 635, 1983.

Mizera, P. F., J. F. Fennell, D. R. Croley, A. L. Vampola, F. S. Mozer, R. B. Torbt, M. Temerin, R. Lysak, M. Hudson, C. A. Cattell, R. G. Johnson, R. D. Sharp, A. G. Ghielemetti, and P. M. Kintner, The aurora inferred from S3-3 particles and fields. J. Geophys. Res., 86, 2329, 1981.

Papadopoulos, K., J. D. Gafey, Jr. and P. J. Palmadesso. Stochastic acceleration of large M/Q ions by hydrogen cyclotron waves in the magnetosphere. Geophys. Res. Lett., 7, 1014, 1980.

Petersen, W. K., R. D. Sharp, E. G. Shelley, R. G. Johnson and H. Balsiger, Energetic ion composition of the plasma sheet. J. Geophys. Res., 86, 761, 1981.

Roux, A., S. Perraut, J. L. Rauch, C. de Villedary, G. Kremser, A. Korth, and D. T. Young, Wave-particle interactions near $He+$ observed on board GEOS-1 and 2. 2. Generation of ion cyclotron waves and heating of H^+ ions, J. Geophys. Res., 87, 8174, 1982.

Sgro A. G., and C. W. Nielson, Hybrid model studies of ion dynamics and magnetic field diffusion during pinch implosions. Phys. Fluids, 19, 126, 1976.

Shelley, E. G., R. D. Sharp, and R. G. Johnson, Satellite observations of an ionospheric acceleration mechanism. Geophys. Res. Lett., 3, 654, 1976.

Tanaka M. and C. C. Goodrich. Simulation study of heavy ion heating by electromagnetic ion cyclotron waves injected by proton temperature anisotropy. Research Report. HIFT-87. Hiroshima Univ.. 1983.

Young. P. T.. Ion composition measurements in magnetospheric modeling. in Quantitative Modeling of Magnetospheric Processes. Geophys. Monogr. Ser.. vol. 21. edited by W.P.lson. pp 340-363. AGU Washington. D.C.. 1979.

Young. D. T.. S. Perrat. A. Roux. C. de Villedary. R. Gendrin. A. Kurth. G. Kremser and D. Jones. Wave-particle interactions near $He+$ observed on GEOS-1 and -2. 1. Propagation of ion cyclotron waves in He^+-rich plasma. J. Geophys. Res.. 86. 6755. 1981.

Final Report for Air Force Contract

F 19628-82-K-0019

December 1981 - December 1984

1. Papers

1) Sato, T., Excitation of streaming tearing mode, Phys. Rev. Lett., 1982 (in press).

2) Sato, T. and R.J. Walker, Magnetotail dynamics excited by the streaming tearing mode, J. Geophys. Res., 87, A9, 7453, 1982.

3) Ashour-Abdalla, M. and H. Okuda, Plasma physics on auroral field lines: The formation of ion conic distributions, High Latitude Magnetospheric/Ionospheric Plasma Physics, Ed. B. Hultqvist, Plenum Publ. Corp., New York, 1982.

4) Okuda, H. and M. Ashour-Abdalla, Acceleration of hydrogen ions and conic formation along auroral field lines, J. Geophys. Res., 88, 899, 1983.

5) Ashour-Abdalla, M. and H. Okuda, Transverse acceleration of ions on auroral field lines, Energetic Ion Composition of Earth's Magnetosphere, Ed. R.J. Johnson, Terra Scientific Publ. Co., Tokyo, 1983.

6) Sato, T., T. Hayashi, R.J. Walker and M. Ashour-Abdalla, Neutral sheet current interruption and field-aligned current generation by three-dimensional driven reconnection, Geophys. Res. Lett., 10, 3, 221, 1983.

7) Walker, R.J., Modeling planetary magnetospheres, UCLA IGPP preprint 2352, Rev. Geophys. Space Phys., 4, 2, 495, 1983.

8) Terasawa, T., Hall current effect on tearing mode instability, Geophys. Rev. Lett., 10, 6, 475, 1983.

9) Ashour-Abdalla, M. and H. Okuda, Turbulent heating of heavy ions on auroral field lines, J. Geophys. Res., 89, 2235, 1983.

10) Terasawa, T., Reconnection in space plasma, to appear in the Proceedings of the Spring College on Radiation in Plasmas, held at International Centre for Theoretical Physics, Trieste, Italy, June, 1983.

11) Sato, T. and M. Murakami, A numerical model of centrifugal wind in a rapidly rotating magnetosphere, Geophys. Res. Lett., 10, 11, 1120, 1983.

12) Wu, C.C., MHD modeling of the Earth's magnetosphere, to appear in the Proceedings of the First International School for Space Simulation (ISSS), Kyoto, Japan, November, 1982.

13) Walker, R.J. and T. Sato, Externally driven magnetic reconnection, submitted to the Proceedings of the Los Alamos Chapman Reconnection Conference, Geophys. Monograph Series, 1983.

14) Sato, T., Computer modeling of magnetic reconnection - an overview, submitted to the Proceedings of the Los Alamos Chapman Reconnection Conference, Geophys. Monograph Series, 1983a.

15) Sato, T., 3D computer modeling of dayside reconnection, submitted to the Proceedings of the Los Alamos Chapman Reconnection Conference, Geophys. Monograph Series, 1983c.

16) Shigeta, M., T. Sato and B. Dusgupta, Streaming tearing mode, submitted to Phys. Fluids, 1983.

17) Sato, T., R.J. Walker and M. Ashour-Abdalla, Driven magnetic reconnection in three dimension: Energy conversion and field aligned current generation, J. Geophys. Res., 89, 9761, 1984.

18)   Terasawa, T., Hall tearing instability in dissipationless plasmas, submitted to Phys. Res. Lett., 1984.

19)   Gendrin, R., M. Ashour-Abdalla, Y. Omura, and K. Quest, Linear Analysis of Ion Cyclotron Interaction in a Multicomponent Plasma, J. Geophys. Res., 89, 9119, 1984.

20)   Omura, Y., M. Ashour-Abdalla, K. Quest, and R. Gendrin, Heating of thermal helium in the equatorial magnetosphere: A simulation study, J. Geophys. Res., 1984 (in press).

2. Invited Talks

1) M. Ashour-Abdalla, Plasma physics of auroral field lines, Nobel Symposium, Kiruna, Sweden, 1982.

2) T. Sato, Numerical study of magnetic reconnection mechanisms, AGU, Philadelphia, May 1982, (EOS 63, 413).

3) M. Ashour-Abdalla, Transverse acceleration of ions by ion cyclotron waves, Theory Conference on Solar-Terrestrial Physics, Boston College, Chestnut Hill, August 1982.

4) T. Terasawa, Numerical simulation of tearing mode instability, Theory Conference on Solar-Terrestrial Physics, Boston College, Chestnut Hill, August 1982.

5) T. Terasawa, Particle and hybrid simulation of tearing mode instability, The First International School for Space Simulation (ISSS), Kyoto, November 1982.

6) R.J. Walker, MHD modeling of the magnetospheric structure, The First International School for Space Simulation (ISSS), Kyoto, November, 1982.

7) M. Ashour-Abdalla, Turbulent heating of heavy ions, AGU, San Francisco, December 1982, (EOS 63, 1073).

8) T. Terasawa, Hall current effect on tearing mode instability, AGU, San Francisco, December 1982, (EOS 63, 1073).

9) M. Ashour-Abdalla, Simulations of wave-particle interaction in space, Spring College on Radiation in Plasmas, International Centre for Theoretical Physics, Trieste, June 1983.

10) T. Terasawa, Reconnection in space plasmas, Spring College on Radiation in Plasmas, International Centre for Theoretical Physics, Trieste, June 1983.

11) R.J. Walker, Modeling the magnetotail and reconnection, IUGG meeting, Hamburg, 1983.

12) R.J. Walker, Driven magnetic reconnection, Chapman Conference on Reconnection, Los Alamos, 1983.

13) T. Sato, Computer modeling of magnetic reconnection - an overview, Chapman Conference on Reconnection, Los Alamos, 1983.

14) T. Sato, Dayside reconnection, American Geophysical Union, San Francisco, (EOS Trans. AGU, 64, 45, 799, 1983), 1983.

15) M. Ashour-Abdalla, Wave energization, Conference on Planetary Plasma Environments: A comparative view, Yosemite, February 1984.

16) K. Watanabe, M. Ashour-Abdalla and T. Sato, Three-dimensional modeling of the magnetosphere-ionosphere coupling, URSI, Florence, August 1984.

17) C.C. Wu, Structure of the magnetosphere, Chapman Conference on the magnetospheric polar cap, Fairbanks, August 1984.

18) T. Sato, Theoretical bases for the magnetosphere-ionosphere coupling, American geophysical Union, San Francisco, December 1984.

3. Contributed Talks

1) Sato, T., T. Hayashi, R.J. Walker and M. Ashour-Abdalla, Neutral sheet current interruption and field aligned current generation by three-dimensional driven reconnection, IUGG meeting, Hamburg, 1983.

2) Terasawa, T., "Hall-tearing" instability in two-dimensional plasma sheet, American Geophysical Union, San Francisco (EOS Trans. AGU, 64, 45, 819, 1983), 1983.

3) T. Sato, 3D computer modeling of dayside reconnection, Chapman Conference on Reconnection, Los Alamos, 1983.

4) Gendrin, R., M. Ashour-Abdalla, Y. Omura and K. Quest, Acceleration of heavy ions by ULF electromagnetic waves. 1. Analytical study of the linear phase, American Geophysical Union, San Francisco, (EOS Trans. AGU, 64, 45, 815, 1983), 1983.

5) Y. Omura, M. Ashour-Abdalla, R. Gendrin and K. Quest, Acceleration of heavy ions by ULF electromagnetic waves. 2. Simulation results, American Geophysical Union, San Francisco, (EOS Trans. AGU, 64, 45, 815, 1983), 1983.

6) Berchem, J., R. Gendrin and M. Ashour-Abdalla, Acceleration of heavy ions by ULF electromagnetic waves. 3. Analytical study of the nonlinear phase, American Geophysical Union, San Francisco, (EOS Trans. AGU, 64, 45, 815, 1983), 1983.

7) Watanabe, K., T. Sato and M. Ashour-Abdalla, 3D model of magnetosphere-ionosphere feedback interactions in the auroral region, American Geophysical Union, San Francisco, (EOS Trans. AGU, 64, 45, 800, 1983), 1983.

8) Watanabe, K., T. Sato, and M. Ashour-Abdalla, Numerical simulation of auroral arc formation due to magnetosphere-ionosphere feedback interactions, American Geophysical Union, Cincinnati, May 1984.

9) Ogino, T., An MHD simulation of bifurcation of tail lobes during intervals with northward IMF, American Geophysical Union, Cincinnati, May 1984.

10) Hada, T. and T. Terasawa, Nonlinear evolution of low frequency waves in the foreshock region of earth's bow shock, American Geophysical Union, Cincinnati, May 1984.

11) Ogino, T. and R.J. Walker, An MHD simulation of the bifurcation of tail lobes during intervals with northward IMF, Chapman Conference on the Magnetospheric Polar Cap, Fairbanks, August 1984.

12) Ashour-Abdalla, M., Y. Omura, R. Gendrin and K.B. Quest, Heating of thermal helium in the equatorial magnetosphere: A simulation study, American Geophysical Union, San Francisco, December 1984.

13) Hada, T., Excitation of compressional low-frequency waves in the earth's foreshock, American Geophysical Union, San Francisco, December 1984.

14) Ogino, T., R.J. Walker and M. Ashour-Abdalla, A magnetohydro-dynamic simulation of effects of the interplanetary magnetic field (IMF) component B_y-dependence on the interacvtion of the solar wind with the earth's magnetosphere during intervals with southward IMF, American Geophysical Union, San Francisco, December 1984.

15) Pritchett, P.L., The electron-cyclotron maser instability in relativistic plasmas, American Physical Society, Boston, October 1984.

16) Pritchett, P.L. and R.J. Strangeway, The cyclotron maser instability in relativistic plasmas: Implications for the generation of auroral kilometric radiation, American Geophysical Union, San Francisco, December 1984.

17) Strangeway, R.J. and P.L. Pritchett, Generation of auroral kilometric radiation by weakly relativistic electrons: Wave growth and ray propagation, American Geophysical Union, San Francisco, December 1984.

18) Walker, R.J. and T. Ogino, A magnetohydrodynamic simulation of the interplanetary magnetic field B_y component-dependent magnetospheric convection and field-aligned currents during northward IMF, American Geophysical Union, San Francisco, December 1984.

19) Watanabe, K., M. Ashour-Abdalla, and T. Sato, Three-dimensional modeling of magnetosphere-ionosphere coupling, American Geophysical Union, San Francisco, December 1984.

20) Wu, C.C., Kelvin-Helmholtz instability and the magnetopause boundary layers, American Physical Society, Boston, October 1984.

21) Wu, C.C., Kelvin-Helmholtz instability and the magnetopause boundary layers, American Geophysical Union, San Francisco, December 1984.

END

DTIC

9- 86